This is a post-peer-review, pre-copyedit version of an article published in
Theor. Comput. Fluid Dyn. The final authenticated version is available online at:
http://dx.doi.org/10.1007/s00162-018-0468-y

Thermodynamic fluctuations in canonical shock-turbulence interaction: effect of shock-strength

Yogesh Prasaad M. Sethuraman · Krishnendu Sinha · Johan Larsson

Received: date / Accepted: date

Abstract In this work, we use numerical simulation and linear inviscid theory to study the thermodynamic field generated by the interaction of a shock wave with homogeneous isotropic turbulence. Fluctuations in density, pressure, temperature and entropy can play an important role in shock-induced mixing, combustion and energy transfer processes. Data from shock-captured direct numerical simulation (scDNS) is used to investigate the variation of thermodynamic fluctuations for varying shock strengths, and the results are compared with linear interaction analysis (LIA). The density, pressure and temperature variances attain large values at the shock, followed by, in general, a rapid decay in the downstream flow. The rapid variation behind the shock makes it difficult to compare numerical results with theoretical predictions. A threshold method based on instantaneous shock dilatation is used to overcome this problem, and it gives excellent match between scDNS and LIA. We find cases with non-monotonic variation with Mach number as well as local peaks in density fluctuations behind the shock. These are explained in terms of the contribution of the post-shock acoustic and entropy modes in the LIA solution and their cross-correlation. Budget of the transport equations reveal interesting insight into the physics governing the thermodynamic field behind the shock wave. It is found that the variances are primarily determined by the competing effects of dilatational and dissipation mechanisms. The dominant mechanisms are identified for a range of conditions and their implication for developing predictive models is highlighted.

Keywords compressible flows · homogeneous turbulence · shock waves

Y. P. M. Sethuraman
Department of Aerospace Engineering, Indian Institute of Technology Bombay, Mumbai, India 400 076.
E-mail: yogesh@aero.iitb.ac.in

Krishnendu Sinha
Department of Aerospace Engineering, Indian Institute of Technology Bombay, Mumbai, India 400 076.
E-mail: krish@aero.iitb.ac.in

Johan Larsson
Department of Mechanical Engineering, University of Maryland, College Park, MD, USA 20742.
E-mail: jola@umd.edu

1 Introduction

Shock waves are characteristic features in high-speed compressible turbulent flows, specifically in the supersonic/hypersonic flow regime. In aerospace applications, the effect of shock waves on the turbulent features in a supersonic boundary layer is usually studied to understand the physical mechanisms responsible for boundary layer separation, increased heat transfer and high surface pressures, each of which are unique engineering problems. The interaction of free turbulence with a planar shock wave is a similar problem of interest, rich with physical insights on the effects of shock on turbulence and vice-versa without additional complexities such as mean shear, streamline curvature and wall effects. Shock-turbulence interaction has implications in a variety of applications, to name a few, supersonic/hypersonic propulsion systems, inertial confinement fusion, shock wave lithotripsy, and astrophysical shock waves. In this study, we focus on the interaction of a homogeneous isotropic turbulence interacting with a nominally planar shock wave, which is the most basic form of shock-turbulence interaction.

Initial studies of shock-turbulence interaction were theoretical, mostly employing linear analysis and were based on the Kovásznay's decomposition of turbulence [23]. The theory aptly called as the linear interaction analysis was developed by [38] and [45] to analyze the interaction of acoustic and vorticity waves respectively with an unsteady normal shock. The theory was later made use of by many researchers to study problems involving shocks and free turbulence [31, 29, 30, 35, 37, 36, 9, 11, 56, 18, 17]. Recently, [43] studied the interaction of purely vortical turbulence with a normal shock using LIA and data from the DNS of [26] for understanding the turbulent heat flux correlation. The linear theory has been used towards development of simple turbulence models which represent the underlying flow physics [51, 50, 41].

A number of physical experiments utilizing grid-generated turbulence interacting with a normal shock have been carried out [15, 19, 16, 3, 2] to study the underlying mechanisms responsible for amplification of turbulent kinetic energy (TKE) and the modification of length scales across the shock; purely driven by the need to understand mixing enhancement across the shock and shock wave/turbulent boundary layer interaction (SBLI). Several numerical simulations have been carried out to study the canonical shock-turbulence interaction problem due to its geometric simplicity and rich physics. Shock-resolved simulations (viscous shock-profile is resolved) [31, 29, 20, 48, 34], shock-captured simulations (shock-profile is numerically estimated) [14, 30, 36, 27, 26], and shock-fitting simulations (shock thickness is neglected by specifying Rankine-Hugoniot conditions) [49, 44, 55] have been carried out to study this problem. The focus has been to understand the amplification of TKE and enstrophy, reduction in length scales, and enhanced anisotropy in post-shock Reynolds stresses.

Compressible turbulent flows are characterized by appreciable changes in thermodynamic quantities such as density, pressure and temperature fluctuations, which can be drastically amplified / altered on interaction with shock waves. The importance of understanding the thermodynamic fluctuations is well known as they play a major role in turbulent mass flux, sound generation, turbulent heat flux, and most importantly, in the turbulent transport of energy between internal and kinetic energy components [33]. For example, in the process of inertial confinement fusion, the mixing of fuel layers is aided by the Rayleigh-Taylor instability (RTI) or the Richtmyer-Meshkov instability (RMI) of the interface between two fluids (as the case maybe), induced by the traveling shock wave. The amount of density variations describe the turbulent mass flux in the interface which in turn determines the degree of mixing between the fluids. In a similar way, the density variations in the interstellar medium due to accelerating astrophysical shocks (induced by supernovae explosions) is widely studied to understand the evolution of various cosmic phenomena (see [57,1] and related works). An understanding of the generation of pressure fluctuations behind the shock in a supersonic over-expanded nozzle (e.g., rocket nozzles of space vehicles) is necessary to mitigate jet noise. In a similar vein, temperature fluctuations (and its gradients) determine the localized surface heat transfer rates at shock impingement point in aerospace vehicles.

The majority of earlier works have focused on velocity fluctuations and its related statistics with limited and sparse data on thermodynamic fluctuations. Lee et al. performed shock-resolved DNS (srDNS) [31,29] at low Mach numbers (1.05 - 1.20) and shock-captured DNS (scDNS) [30] at high Mach numbers (2 and 3) to study the amplification of turbulence behind the shock. They found that the post-shock thermodynamic state is nearly isentropic for the weak-shock interactions and follow a polytropic (and non-isentropic) scaling for strong interactions. They also studied the budget of terms in the density equation, and found that its evolution behind the shock is dominated by the correlation between density and dilatation fluctuations. Mahesh et al. [37,36] also observed similar amplification of thermodynamic fluctuations across the shock for Mach numbers of 1.2 to 1.8, followed by a rapid decay behind the shock. They also found qualitative agreement between LIA and numerical simulations. Additionally, they studied the effect of upstream entropy fluctuations on the post-shock turbulence. Recently, Tian et al. [54] studied the interaction of a Mach 2 shock wave with isotropic turbulence with (multi-fluid) and without (single-fluid) variable compositions. They compared the conditional expectation of density, pressure and temperature fluctuations amongst each other, and found isentropic scaling. In all of the above shock-turbulence interaction (STI) studies, there are no rigorous comparisons between LIA and numerical simulations for the post-shock thermodynamic field, especially for strong shock waves. This work aims to study the amplification of thermodynamic fluctuations across strong shocks and make qualitative as well as quantitative comparisons between LIA and numerical simulations to highlight the predictive capabilities of LIA.

The objective of the present study is to perform a detailed investigation of the thermodynamic aspects of the canonical shock-turbulence interaction. We study the generation of density, pressure, temperature and entropy fluctuations across a shock wave. Studying the four thermodynamic variances will also help explain the behaviour of related quantities, like the turbulent mass flux ($\overline{\rho' u_i'}$) and turbulent heat flux ($\overline{h' u_i'}$), in the flow. Our aim is to fill in the gaps in existing literature, specifically in the high Mach number regime, and to investigate the physics that govern the thermodynamic field behind the shock. We use the extensive scDNS dataset of [26] covering a wide range of Mach numbers, and complement it with additional simulations performed as part of the current work. A wide range of Mach numbers, from low supersonic to hypersonic values are considered. The results are compared with the predictions from linear interaction analysis. Kovásznay mode decomposition of the LIA solution and the budget of transport equations computed using simulation data are used in a complementary way to bring out the dominant physical mechanisms. We will thus lay the foundation for developing advanced physics-based models for shock-turbulence interaction, similar to those in [50,51] and others.

The paper is organized as follows: Sect. 2 introduces the reader to the numerical methodology followed in the current work with verification of the numerical simulations. The salient points of the linear interaction analysis are also described briefly. Sect. 3 presents extensive comparison between the LIA predictions and the data obtained from the current numerical simulations, as well as those of [26]. The thermodynamic variances are plotted as a function of distance from the shock for different Mach numbers, and as a function of Mach number at different spatial locations. The rapid variation of the thermodynamic variances behind the shock makes it difficult to do a meaningful comparison between theory and simulation. These challenges are alleviated by a new threshold method of computing statistics, conditioned on the instantaneous shock location in the numerical simulations. It is based on the concept of near-field in the LIA solution and it shows excellent match between simulation and theory for a range of Mach numbers.

Decomposing the disturbance field into Kovásznay modes of vorticity, entropy and acoustic can provide interesting insight. This proved to be useful in analyzing the peak turbulent heat flux generated by a shock wave in [42], and in developing physics-based model for the same (in [41]). Here, we use Kovásznay mode decomposition to investigate the post-shock evolution of the density and temperature variances. We also compute the budgets of the transport equation for the thermodynamic quantities, using the simulation data generated as part of this work in Sect. 4. The two together help us to identify the dominant physical mechanisms in the flow, and we discuss their modeling implication in Sect. 5. Conclusions are presented in Sect. 6.

We consider a purely vortical incoming turbulence in LIA and mostly vortical with minimal compressible fluctuations in the numerical simulations. The case of vortical upstream turbulence is the most fundamental of all shock-turbulence interactions, and is taken as a starting point for other cases with acoustic or entropy fluctuations upstream of the shock wave. Grid-generated decaying turbulence in the experiments of [19,3,2,22] and many other turbulent flows such as supersonic wall boundary layers (see [39] and related articles) comprise of vortical and acoustic fluctuations. The flowfields with very low M_t are dominated by vorticity fluctuations, and the effects of compressibility are found to be weak [52].

2 Methodology

We present the details of the numerical method, along with the initial and boundary conditions; they are based on previous work by [26]. The test cases of canonical shock-turbulence interaction computed as part of the current work and a detailed grid refinement study are also presented. Post-processing of the simulation data is described and a new threshold method to compute thermodynamic variances close to the instantaneous shock wave is proposed. This is followed by a brief outline of the linear interaction analysis and the Kovásznay mode decomposition of the thermodynamic field generated by the shock interaction.

2.1 Numerical simulations

The compressible Navier-Stokes (NS) equations are solved for a perfect gas with ratio of specific heats $\gamma = 1.4$ and zero bulk viscosity. A linear constitutive equation with Stoke's hypothesis is used for relating the viscous stresses to the strain rates, $\sigma_{ij} = \mu\,(\partial_{x_i} u_j + \partial_{x_j} u_i - 2/3\,\partial_{x_m} u_m\,\delta_{ij})$ and Fourier's law is used for the heat flux, $q_j = -\kappa\,\partial_{x_j} T$. Viscosity is assumed to follow a power-law with temperature as $\mu = \mu_{ref}\,(T/T_{ref})^{3/4}$ (cf. [26] for the expressions). Einstein convention is used for the vectors (and tensors) where the subscripts $i = 1, 2, 3$ correspond to components in x_1, x_2, x_3 directions respectively.

The governing equations are solved using the solution-adaptive finite difference *Hybrid* code [4], which uses a fifth-order WENO scheme with Roe flux-splitting around the shock and a sixth-order central scheme in the "split" form of [8] in the remainder of the domain. The viscous term is computed in a way that is conservative yet has the resolution characteristics of a sixth-order scheme. A shock wave is identified as the region where the negative dilatation is greater than the low pass-filtered vorticity magnitude, i.e., where $-\partial_{x_j} u_j > \sqrt{\omega_j \omega_j}$. The system of equations is integrated in time using a fourth-order accurate explicit Runge-Kutta (RK4) scheme. This numerical procedure has been verified and validated on several problems of interest [21,27,26]. Further details about the code can be found in [27,4] and in [26].

We use the notion of Favre averages (density-weighted) for all quantities from the numerical simulations except for ρ and p. The Favre averages are defined as $\widetilde{f}$ and the associated fluctuations are denoted by double primes (e.g., f''). Reynolds averaged quantities and their fluctuations are denoted by an overbar and single prime respectively.

A homogeneous isotropic turbulence field is generated as per the method given in [27]. The initial fields have decaying velocity spectra of the von Kármán form [25] with peak energy at wavenumber $k_0 = 4$. Compressible fluctuations are added using the "pseudo-sound" relationships provided in [46]. The isotropic databases decay in time till 'realistic' turbulence is obtained, as determined by having decaying enstrophy, velocity derivative skewness settled around -0.5 and an increasing dissipation length scale. The resolution of the resulting database is ensured to satisfy the criterion $k_{max}\eta \geq 1.5$ [27,40], where η is the Kolmogorov length scale and k_{max} is the maximum possible wavenumber. Multiple databases are blended using the method of [24] to form a longer turbulence database. Finally, Taylor's hypothesis is used to specify the homogeneous isotropic database as the time-dependent inflow turbulence for the canonical shock-turbulence interaction problem.

The blending procedure has a very small effect on the realism of the turbulence, and changes the root-mean-square (rms) values of the thermodynamic fluctuations by less than 1% and that of the dilatational fluctuations by 2%. The assumption of Taylor's hypothesis when convecting the inflow database into the domain introduces much larger errors since it is inaccurate for the acoustic waves [28]. For example, it increases the rms of the thermodynamic fluctuations by 5% and that of the dilatational fluctuations by 25%. However, the resulting turbulence is still 99% vortical with only a minimal amount of thermodynamic and dilatational fluctuations. The turbulence database is found to have the following parameters: turbulent Mach number $M_{t,db} = 0.155$ and Taylor microscale Reynolds number of $Re_{\lambda,db} = 34$.

2.1.1 Simulation parameters

Simulations of four different upstream Mach numbers ($M_u = 1.23, 1.50, 2.50$ and 3.50) have been carried out in the present study with constant turbulent Mach number of $M_{t,u} = 0.15$ and Taylor microscale Reynolds number of $Re_{\lambda,u} = 33$. Additionally, the comprehensive statistics from the dataset of [26] with M_u ranging from 1.27 to 6 for varying upstream turbulent Mach numbers (0.15−0.38) and Taylor-scale Reynolds numbers (40 and 75) are also used when presenting the results. Subscripts u and d denote upstream and downstream states respectively.

Figure 1 shows the schematic of the computational domain with the shock-normal direction aligned with the streamwise direction (x_1). The computational domain is $k_0 L_{x_1} = 9\pi$ long in the streamwise direction with the shock initially placed at $k_0 x_1 = 1\pi$, and is of length $k_0 L_{x_2} = k_0 L_{x_3} = 8\pi$ in the shock-parallel directions. An optimized numerical sponge is attached at the end of the domain to gradually dissipate the spurious oscillations from the outflow. A non-reflecting boundary condition is used at the outflow along with periodic boundary conditions for the shock-parallel directions (x_2 and x_3). A back pressure controller as per the method provided in [27] is also employed to adjust the mean shock position. The mean shock drift speed, $\overline{u}_s < 0.0002\,\overline{u}_{1,u}$ for all cases in the present study.

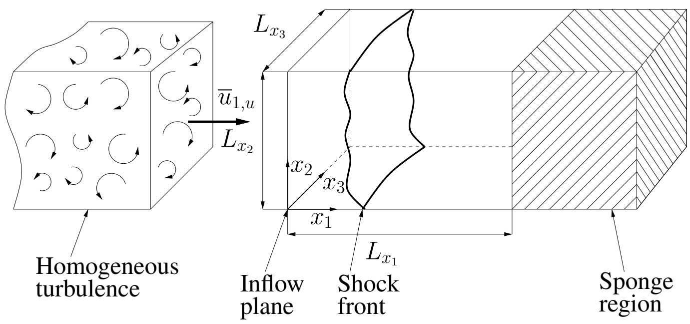

Fig. 1 A schematic of the shock-turbulence interaction computational domain used in the numerical simulations

The computational grid is stretched in the shock-normal direction to facilitate finer grid sizes near the shocks and relatively coarser sizes away from the shock. A uniform grid spacing is used for the shock-parallel directions. The grid sizes are varied to ensure that the anisotropically compressed post-shock turbulence [27] is captured as the shock strength varies between the cases.

Table 1 provides the necessary details on lengthscales and the grid resolution for all of the cases including the cases considered in grid convergence tests (discussed in Sect. 2.1.2). The upstream shock-turbulence intensity given by $M_{t,u}/(M_u - 1)$ varies from 0.65 to 0.06 which shows that the $M_u = 1.23$ case is in the 'broken shock' regime and the remaining cases are in the 'wrinkled shock' regime [6,7,26]. The reduction in Kolmogorov lengthscale is described with respect to the numerical shock thickness (δ_n) [54] in the sixth and the seventh columns of the table respectively. The pre-shock Kolmogorov lengthscale varies from $0.7 - 1.3$ times the numerical shock thickness for the cases considered here and the post-shock Kolmogorov lengthscale is about half the numerical shock thickness. The normalized Kolmogorov lengthscale, $k_{max}\eta$ is usually taken to be ≥ 1.5 to resolve small-scale turbulence [40]. The post-shock Kolmogorov lengthscale based on the largest grid size among all three directions defined as $(k_{max}\eta)_{min}$ [54] (eighth column in the table) is satisfied for the low Mach number cases ($M_u = 1.23$ and 1.50) and is marginally less for the high Mach number cases of 2.50 and 3.50.

We show by a detailed grid convergence test (Sect. 2.1.2) that the chosen grid sizes for each of the case are sufficiently resolved for the statistics considered here. In all the cases, the ratio of the post-shock dissipation lengthscale to the Kolmogorov lengthscale ($L_{\epsilon,d}/\eta_d$) is > 40, which is sufficiently large enough to resolve the large scale quantities [26], such as Reynolds stress. The last column provides the ratio of upstream Kolmogorov lengthscale (η_u) to the viscous shock thickness (δ_s) [48] which provides an estimate for the difference in grid-spacing resolution between the shock-captured simulations in the current study and their corresponding shock-resolved simulations. The ratio of numerical shock thickness to the viscous shock thickness in the post-shock region is approximately 3 for the low Mach number cases and 10 for the high Mach number cases, assuming that the viscous shock formulation can also be applied to the stronger shocks. The statistics for the current simulations are computed by averaging over a time period of one flow-through time of the turbulence database (τ_{db}), which is 8 isotropic boxes long.

2.1.2 Verification

Grid convergence test for various statistics has been carried out for the case of $M_u = 1.50$ and 3.50 with $M_{t,u} = 0.15$ and $Re_{\lambda,u} = 33$ using grids varying from 256 to 512 grid points in the shock-parallel directions. Larsson and Lele [27] noted that the Kolmogorov lengthscale decreases behind the shock due to the increase in the viscous dissipation rate, which implies that the grid size behind and at the shock should be refined sufficiently to resolve the shock-modified turbulence. The grid aspect ratio (GAR) at the shock (given by $\Delta x_{1,s}/\Delta x_{2/3}$) has been varied to resolve the reduction in Kolmogorov lengthscale behind the shock. In the present work, the GAR at the shock is estimated using the relation $\eta_d/\eta_u \approx (T_d/T_u)^{3/8}(\rho_d/\rho_u)^{-1} \approx \Delta x_{1,s}/\Delta x_{2/3}$ provided in [27]. Recently, Tian et al. [54] computed the numerical shock thickness as $\delta_n = (u_{1,u} - u_{1,d})/|\partial u_1/\partial x_1|_{max}$, and noted that there are no significant errors in

[a] Ratio of viscous shock thickness to Kolmogorov lengthscale, $\delta_s/\eta \approx 7.69 M_{t,u}/(\sqrt{Re_{\lambda,u}}(M_u - 1))$ [48]. This formulation is not valid for $M_u > 2$ [53]

Table 1 List of cases simulated in the present study including the cases considered in grid convergence tests. $\Delta x_{2/3}$ is the transverse grid spacing, $\Delta x_{1,s}$ is the shock-normal grid spacing at the shock, δ_n is the numerical shock thickness, δ_s is the viscous shock thickness and η is the Kolmogorov lengthscale. Note that k_{max} is based on the transverse grid-spacing. Cases denoted by bold characters are the finalized cases used for presenting the results

Case	M_u	$\frac{M_{t,u}}{(M_u-1)}$	Grid	$\Delta x_{2/3}/\Delta x_{1,s}$	η_u/δ_n	η_d/δ_n	$(k_{max}\eta)_{min}$	η_u/δ_s [a]
1.23	**1.23**	**0.65**	$\mathbf{882 \times 384^2}$	**1.66**	**0.71**	**0.57**	**2.38**	**1.11**
1.5*a*	1.50	0.30	695×256^2	2.00	0.55	0.36	1.30	2.44
1.5*b*	1.50	0.30	522×384^2	1.00	0.45	0.30	1.98	2.44
1.5c	**1.50**	**0.30**	$\mathbf{1042 \times 384^2}$	**2.00**	**0.95**	**0.61**	**1.91**	**2.44**
1.5*d*	1.50	0.30	1566×384^2	4.00	1.69	1.08	1.90	2.44
1.5*e*	1.50	0.30	1390×512^2	2.00	1.15	0.75	2.55	2.44
2.50	**2.50**	**0.10**	$\mathbf{1142 \times 384^2}$	**2.50**	**1.18**	**0.56**	**1.40**	**7.14**
3.5*a*	3.50	0.06	875×256^2	3.03	0.72	0.33	0.90	12.5
3.5*b*	3.50	0.06	658×384^2	1.51	0.64	0.30	1.39	12.5
3.5c	**3.50**	**0.06**	$\mathbf{1313 \times 384^2}$	**3.03**	**1.30**	**0.58**	**1.32**	**12.5**
3.5*d*	3.50	0.06	1844×384^2	6.25	2.50	1.11	1.30	12.5
3.5*e*	3.50	0.06	1750×512^2	3.03	1.36	0.61	1.71	12.5

the post-shock statistics when the numerical shock thickness is 1.4 times smaller than the Kolmogorov lengthscale. Boukharfane et al. [5] used grid spacing which is $4-8$ times smaller than η_u at the shock, and found similar results as in [54]. We show by a thorough grid refinement test that these values are not universal, and are dependent on the numerical methodology adopted.

Figure 2a shows negligible differences ($\approx 2\%$) in the post-shock values of the Kolmogorov lengthscale as the grid spacing is refined in the shock-normal direction. Figure 2b shows the ratio of Kolmogorov lengthscales as a function of shock strength obtained from the numerical simulations which closely follows the estimate obtained using the expression given in [27]. We observed that the estimate given in [27] to be sufficient (with a variation of 10%) for determining the required grid spacing in the shock-normal direction *a priori*. However, the importance of a thorough grid refinement test cannot be understated.

Figures 3 and 4 shows the grid convergence of statistics of interest for the case of $M_u = 3.50$, $M_{t,u} = 0.15$ and $Re_{\lambda,u} = 33$. The large-scale features such as Reynolds stresses ($R_{\alpha\alpha} = \widetilde{u''_\alpha u''_\alpha}$) and small-scale features such as the transverse vorticity variances ($\overline{\omega'_3\omega'_3}$) and the dissipation rate of TKE ($\epsilon = \overline{\sigma_{ij}\partial_{x_j} u''_i}$) are shown in Fig. 3. The grid convergence of the thermodynamic variances are shown in Fig. 4. The maximum difference in various statistics between grid sizes mentioned in 3.5*c*, 3.5*d* and 3.5*e* is found to be $\leq 2\%$. We find similar error values ($\leq 2\%$) between cases 1.5*c*, 1.5*d* and 1.5*e* (not shown). The corresponding case from Larsson et al. [26] is also plotted for the available Reynolds numbers of $Re_{\lambda,u} = 40$ for comparison. There is a clear effect of the shape of the upstream turbulence energy spectrum in the region $k_0 x_1 < 6$. The reader is referred to [43] for more details on the effect of upstream turbulence energy spectrum.

We present the results from the cases of 1.23, 1.5*c*, 2.5 and 3.5*c* provided in Table 1 only in the subsequent sections. We found that the present numerical method

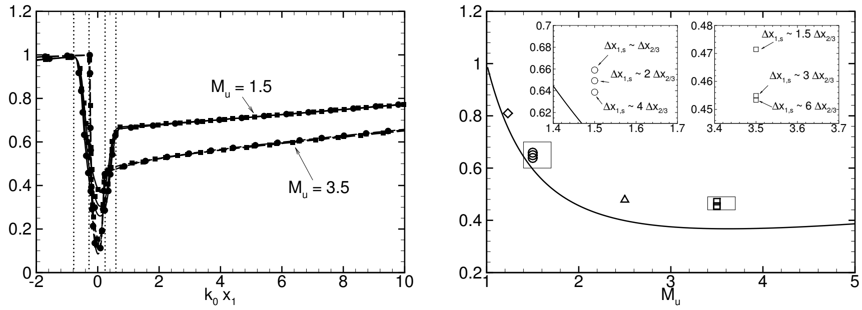

(a) η_d/η_u against $k_0 x_1$ (b) η_d/η_u against M_u

Fig. 2 Variation of the Kolmogorov lengthscale ratio (η_d/η_u) (a) as a function of the shock-normal direction for the cases mentioned in Table 1: 1.5b (solid line with squares), 1.5c (solid line), 1.5d (solid line with circles), 3.5b (dashed line with squares), 3.5c (dashed line), 3.5d (dashed line with circles). The vertical lines around $k_0 x_1 = 0$ show the mean shock thickness for each of the cases where the Mach 3.5 case has the shortest thickness, and (b) as a function of the upstream Mach number with symbols representing the values from the numerical simulations and the solid line represents the estimate for η_d/η_u given in [27]

produces very thin numerical shocks with refinement in the shock-normal grid spacing but very less changes in the post-shock turbulence. In a similar vein, we find the cases 1.5c and 3.5c to be grid-converged with the cases 1.5d, e and 3.5d, e respectively, though the former does not meet the scale separation criterion ($\eta/\delta_n \geq 1.4$ [54]).

2.1.3 Statistics at the instantaneous shock

The different statistics presented in Figures 3 and 4 are computed at fixed x_1 by averaging over the transverse planes for a number of flow realizations. This conventional averaging gives a mean shock thickness determined by the unsteady oscillations of the shock. The turbulent statistics computed in the region of unsteady shock is governed by the Rankine-Hugoniot jump values across the unsteady shock wave. Larsson et al. [26] showed the contribution of the unsteady shock oscillations for the shock-normal Reynolds stress to be very large inside the shock. This effect is also seen in other statistics and the values are found to be large if one would compute them at the edges of the mean shock. By comparison, statistics conditioned by the local position of the instantaneous shock wave, is unaffected by the shock oscillations.

We employ a novel method to compute statistics at the instantaneous shock locations instead at the edge of the mean shock location. A threshold value based on the instantaneous dilatation is used to identify the shock thickness in the flowfield. This is similar to the dilatation-based shock-sensors used in the simulation, but in a much simpler form. A threshold value of 1% of the most negative dilatation in an instantaneous flow field is used (see Fig. 5b) to identify the bounds of the shock ($x^i_{s,u}$, $x^i_{s,d}$). The instantaneous numerical shock thickness is much smaller than the mean shock thickness (see Fig. 5a) defined by ($\overline{x}_{s,u}, \overline{x}_{s,d}$). The post-shock statistics are then computed by obtaining values at the downstream edge ($x^i_{s,d}$) of the instantaneous

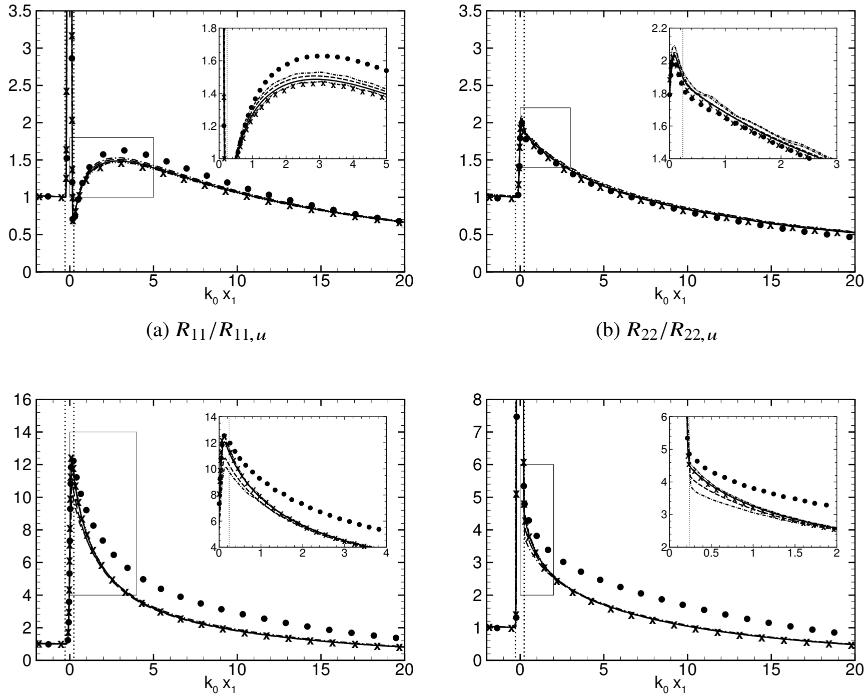

(a) $R_{11}/R_{11,u}$ (b) $R_{22}/R_{22,u}$

(c) $\overline{\omega_3'^2}/\overline{\omega_{3,u}'^2}$ (d) ϵ/ϵ_u

Fig. 3 Grid convergence for the case of $M_u = 3.50$, $M_{t,u} = 0.15$ and $Re_{\lambda,u} = 33$ on the grids 875×256^2 (dashed), 658×384^2 (dash-dotted), 1313×384^2 (solid), 1844×384^2 (x symbols), 1750×512^2 (dash-double dotted): (a) shock-normal Reynolds stress; (b) transverse Reynolds stress; (c) transverse vorticity variance; (d) dissipation rate of TKE. All the quantities are normalized by their corresponding values upstream of the shock. Corresponding data from [26] for the case of $M_u = 3.50$, $M_{t,u} = 0.15$ and $Re_{\lambda,u} = 40$ (circles) is also plotted for comparison. Inset shows the variation in the short region enclosed by the rectangle. Vertical dotted lines around $k_0x_1 = 0$ denote the region of unsteady shock movement

shock wave for each (x_2, x_3, t), and then by averaging suitably. This corresponds to the near-field location defined in linear interaction analysis (discussed below) and is denoted by $k_0x_1 = 0^+$. Using this procedure, termed as the threshold method, we get finite values of the post-shock variances, instead of the very large values obtained in the conventional averaging method due to the inherent effect of unsteady shock oscillations (for example, Fig. 4b). We have assessed the accuracy/convergence of the method and found it to be about 10%.

2.2 Linear interaction analysis

Linear interaction analysis is a theoretical tool, generally used to analyze the shock-turbulence interaction problem. Initially framed by [38] and [45], the tool has been extensively used and developed further by many [37, 9, 11, 56, 18, 17, 43, 42]. The anal-

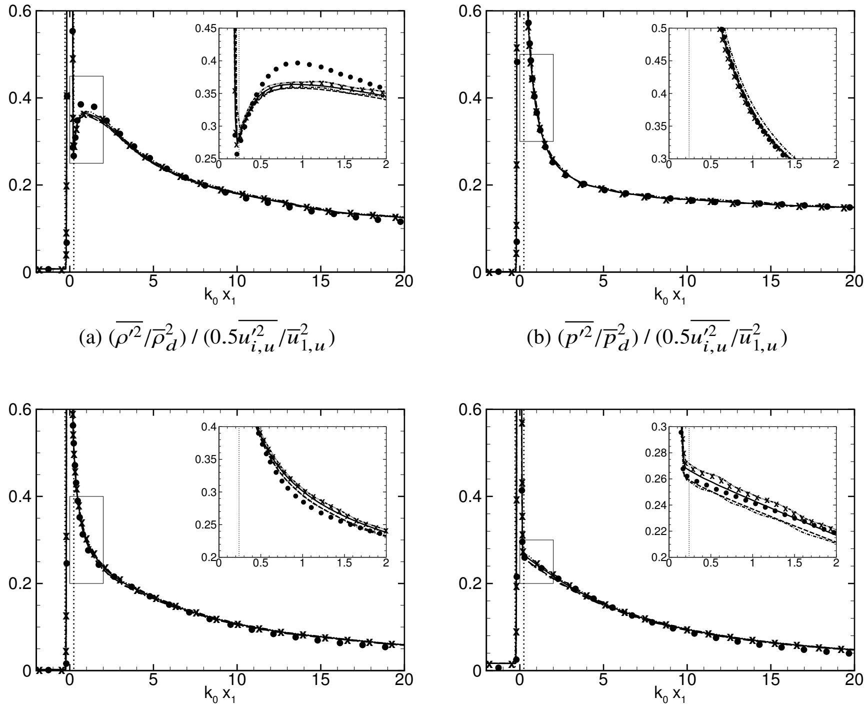

(a) $(\overline{\rho'^2}/\overline{\rho}_d^2)$ / $(0.5\overline{u'^2_{i,u}}/\overline{u}^2_{1,u})$ (b) $(\overline{p'^2}/\overline{p}_d^2)$ / $(0.5\overline{u'^2_{i,u}}/\overline{u}^2_{1,u})$

(c) $(\widetilde{T''^2}/\widetilde{T}_d^2)$ / $(0.5\overline{u'^2_{i,u}}/\overline{u}^2_{1,u})$ (d) $(\widetilde{s''^2}/c_p^2)$ / $(0.5\overline{u'^2_{i,u}}/\overline{u}^2_{1,u})$

Fig. 4 Same as Fig. 3 but shown for thermodynamic variances. (a) density variance; (b) pressure variance; (c) temperature variance; (d) entropy variance. All the quantities are normalized by the square of their corresponding mean values downstream of the shock ($\overline{\rho}_d$, $\overline{p}_d$ and $\overline{T}_d$) except for the entropy variance which is normalized by the square of the gas specific heat capacity at constant pressure (c_p). The quantities are additionally scaled by the normalized TKE $(0.5\overline{u'^2_{i,u}}/\overline{u}^2_{1,u})$. Lines and symbols are as mentioned in the caption of Fig. 3 with the insets showing the short region enclosed by the rectangle

ysis relies on the assumptions that the characteristic length and time scales associated with the shock are very small compared to that of the turbulence, and that the amplitude of the fluctuations in the flow field upstream of the shock are small compared to the mean state.

A single vorticity wave in two-dimensions (x_1, x_2) of amplitude A_v whose wavenumber vector $\mathbf{k}$ is inclined at an angle ψ with the x_1 direction is being convected by a one-dimensional (1D) uniform mean flow of velocity $\overline{u}_{1,u}$ towards the normal shock as shown in Fig. 6a. The shock deforms in response and the position of the unsteady shock is given by $\xi(x_2, t)$.

The generated acoustic waves are inclined at an angle $\widetilde{\psi}$ and the entropy waves are at an angle $\overline{\psi}$ in the downstream region. The refracted vorticity wave is aligned in the same direction as the entropy wave. The wavenumber vector of the acoustic wave is represented by $\widetilde{\mathbf{k}}$ and that of the non-acoustic wave is given by $\overline{\mathbf{k}}$. The post-shock

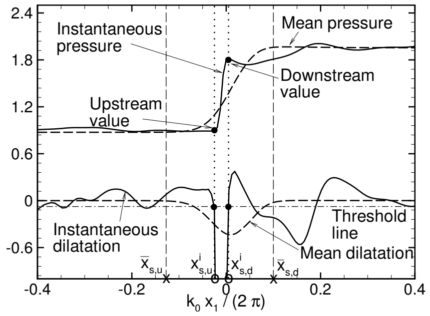

(a) Representative schematic showing the mean and the instantaneous shock thickness

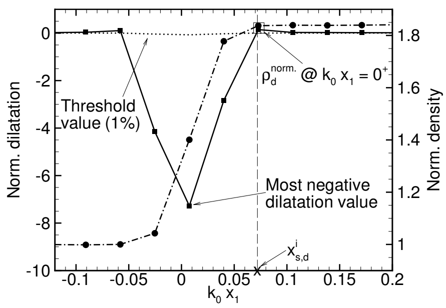

(b) Instantaneous profiles from a flowfield

Fig. 5 Schematic of the threshold method for obtaining near-field values. (a) Representative schematic showing instantaneous (solid lines) and mean (dashed lines) profiles. The dilatation value used as the threshold to identify the extent of the instantaneous shock is shown by a horizontal dash-dotted line. The vertical dashed lines represent the mean shock thickness and the vertical dotted lines represent the instantaneous shock thickness. The edges of the instantaneous shock are denoted by $(x^i_{s,u}, x^i_{s,d})$ and that of the mean shock are shown by $(\overline{x}_{s,u}, \overline{x}_{s,d})$. (b) Schematic reproduced from a flowfield in the case of $M_u = 1.50$, $M_{t,u} = 0.15$ and $Re_{\lambda,u} = 33$. Dilatation (solid line with squares) is normalized by $k_0\overline{u}_{1,u}$ whose scale is given at the left axis. Density (dash-dotted line with circles) is scaled by $\overline{\rho}_u$ and its values are given at the right axis. The symbol x marks the instantaneous downstream location $(x^i_{s,d})$ obtained using the 1% threshold value, and is extended to the density curve by a thin dashed line. The grid point enclosed by the hollow rectangle is the location from which the values are computed as $k_0x_1 = 0^+$ (or near-field) values

acoustic waves can be either propagating or decaying depending on the angle of the incident wave. There exists a critical angle ψ_c for $\psi \in [0, \pi/2]$ beyond which the acoustic waves decay immediately behind the shock.

The linearized Euler equations are solved to study the interaction between isotropic turbulence and the normal shock wave, which is modeled as a discontinuity. Linearized Rankine-Hugoniot (RH) conditions are used as the boundary conditions at the shock wave to obtain the post-shock field. The upstream turbulence is represented as a superposition of plane waves (Fourier modes), with each of them independently interacting with the shock. The two-dimensional (2D) single wave analysis is then extended to the analysis of three-dimensional (3D) isotropic turbulence interacting with the normal shock by making use of the axisymmetric nature of the problem. A cylindrical coordinate system is adopted for the 3D analysis with the incident wavenumber vector lying in the $\mathbf{e}_x - \mathbf{e}_r$ plane and this plane makes an angle ϕ with the x_3 direction as shown in Fig. 6b. The post-shock field thus obtained is then integrated over all of the incident waves to obtain a statistical description of the turbulence behind the shock wave. The turbulence statistics are functions of the distance behind the shock wave, the Mach number of the upstream mean flow, and the incident turbulence energy spectrum. LIA predicts a jump in the turbulent fluctuations across the shock discontinuity, followed by an adjustment region. The inviscid adjustment is a result of the decaying acoustic energy corresponding to the elementary wave interactions with $\psi > \psi_c$, and is described in [43]. The turbulent statistic computed at $x_1 = 0^+$,

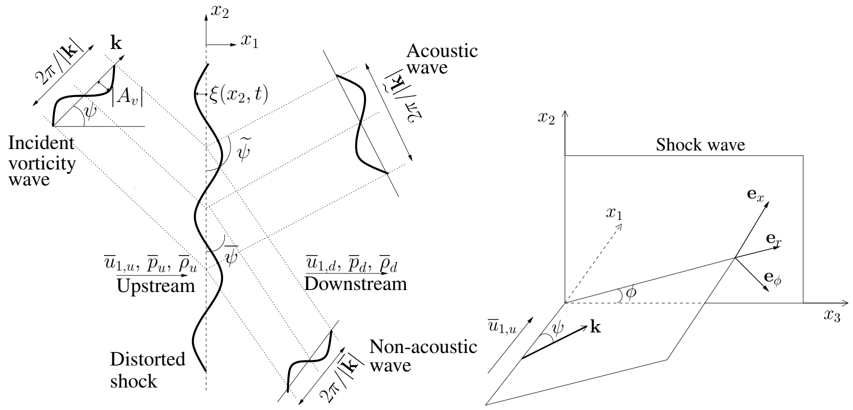

(a) Single wave interaction (b) Coordinate system for 3D interaction

Fig. 6 Linear interaction analysis framework to study the interaction of isotropic turbulence with a normal shock. (a) Schematic of a single vorticity wave interacting with a normal shock and yielding three types of Kovásznay's linear waves. (b) Coordinate system used in the 3D analysis of the interaction of isotropic turbulence with a steady shock wave

immediately behind the shock is termed as the LIA near-field value, whereas the $x_1 \to \infty$ asymptotic values are called LIA far-field.

2.2.1 Kovásznay modes

Kovásznay showed that small perturbations in a compressible turbulent flow can be decomposed into vortical, entropy and acoustic components, which evolve independently in the linear inviscid limit. This forms the foundation of the LIA framework, and is used here to decompose the post-shock thermodynamic fluctuations namely, density (ρ'), pressure (p'), temperature (T'), and entropy (s') into their respective component modes. The objective is to use the modal decomposition to gain insight into the thermodynamic fluctuations generated behind the shock wave and their variation with the shock Mach number.

The post-shock thermodynamic field is due to the acoustic and the entropy modes generated by the shock wave. The acoustic mode consists of isentropic pressure, density and temperature fluctuations, and a dilatational velocity field. The entropy mode, on the other hand, consists of isobaric temperature and density fluctuations. The post-shock entropy fluctuations therefore correspond to a pure mode, and the pressure fluctuations generated at the shock are taken to be entirely due to the acoustic mode.

We note that the different Kovásznay modes are governed by different physical processes. Hence, identifying the modal contributions allows us to investigate the physics behind the observed trends in the post-shock thermodynamic field. A similar Kovásznay mode decomposition of the turbulent energy flux generated by a shock wave is reported in [42], where the modal decomposition is used to investigate the peak positive turbulent energy flux in the post-shock flow. The modal contributions are also used successfully to develop advanced turbulence models for the turbulent heat flux in canonical shock-turbulence interaction [41] and a variable turbulent Prandtl number model for shock-boundary layer flows [47].

The LIA solution in the post-shock region is a superposition of acoustic, entropy and vorticity waves (denoted by subscripts a, e and v respectively), with a collection of orientation angles and wavelengths. The density variance is thus (since the pure vorticity contribution, $\rho'_{d,v} = 0$),

$$\overline{\rho'_d \rho'_d} = \overline{(\rho'_{d,a} + \rho'_{d,e})^2} = \overline{\rho'_{d,a} \rho'_{d,a}} + \overline{\rho'_{d,e} \rho'_{d,e}} + 2\, \overline{\rho'_{d,a} \rho'_{d,e}} \tag{1}$$

which allows us to decompose the full density variance into a pure acoustic contribution (the first term), a pure entropy contribution (the second term), and a combined acoustic/entropy contribution (the third term). These correlations are hereby denoted as aa, ee, ae respectively. A similar decomposition is done for all other quantities. Further details about this decomposition procedure can be found in [42] and in [37].

2.2.2 Convergence to LIA values

Scale separation (defined as η_u/δ_s) poses a physical problem in shock-resolved simulations and is necessary to ensure that the shock width and the turbulence scales do not overlap. In the shock-capturing simulations where the viscous shock profile is replaced by a numerical shock, a large scale separation would imply that the numerical shock-capturing methodology does not alter the post-shock turbulence i.e., the turbulence is resolved albeit the shock is captured [30,26]. Recently, Tian et al. [54] discussed extensively on this scale separation ratio (defined as η_u/δ_n) and used the ratio as a measure to verify the shock-capturing framework of numerical simulations. By systematic variation of M_t and Re_λ, Tian et al. [54] were able to show convergence of Reynolds stresses obtained from shock-captured simulations to the LIA solutions which are also in agreement with the results of low $M_{t,u}$ shock-resolved simulations of [48]. Boukharfane et al. [5] took a different approach where they used the similarity scaling of Donzis [6,7] to show scale separation in their simulations and subsequently, the convergence towards LIA solutions.

The present simulations are for a constant $M_{t,u}$ and $Re_{\lambda,u}$ values, making it difficult to check for convergence to LIA values. We therefore use the dataset of Larsson et al. [26] for verifying the convergence to LIA results, since the same numerical methodology was used in their work. We adopt the approach of [54] to discuss on the convergence to LIA values as $M_{t,u} \to 0$ (negligible nonlinearity) and $Re_{\lambda,u} \to \infty$ (towards inviscid limit) for the numerical methodology used in the current work. Figure 7 shows the convergence of different statistics towards the LIA values as the upstream turbulent Mach number ($M_{t,u}$) is reduced for the case of $M_u = 1.50$ and $Re_{\lambda,u} = 40$. The convergence towards LIA indicates that there exists a sufficient scale separation between the shock wave and the incoming turbulence [48,34,54], even for the low Taylor-scale Reynolds number considered in the study. The results from the datasets of [26] are also presented in [5] as a function of the scaling parameter provided in [6,7] where they have also showed a similar convergence to the LIA solution as the scaling parameter ($M_{t,u}/[Re_{\lambda,u}^{0.5}(M_u - 1)]$) is reduced.

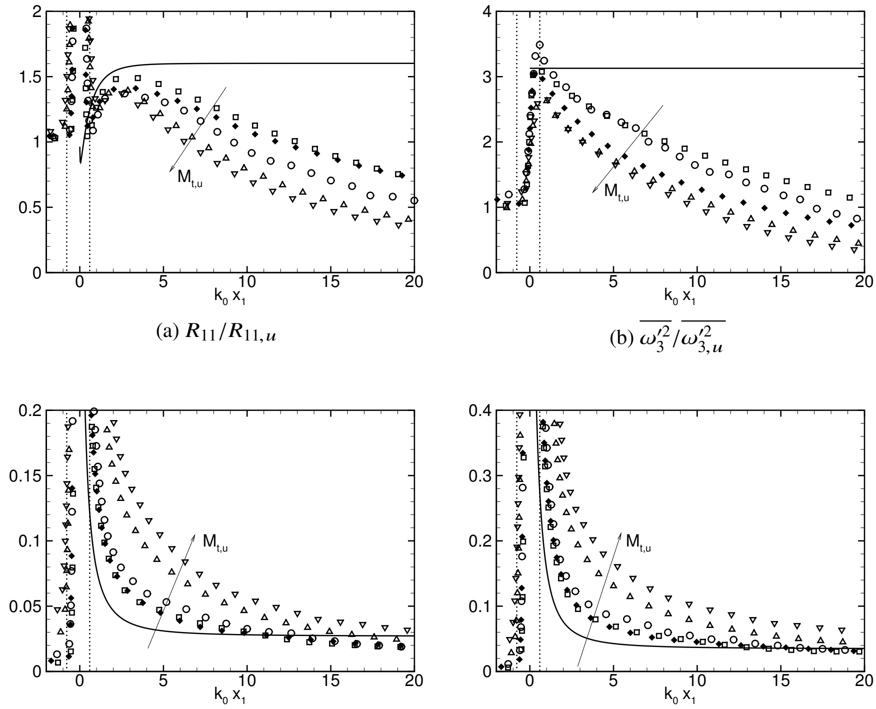

(a) $R_{11}/R_{11,u}$

(b) $\overline{\omega_3'^2}/\overline{\omega_{3,u}'^2}$

(c) $(\overline{\rho'^2}/\overline{\rho}_d^2)$ / $(0.5\overline{u_{i,u}'^2}/\overline{u}_{1,u}^2)$

(d) $(\overline{p'^2}/\overline{p}_d^2)$ / $(0.5\overline{u_{i,u}'^2}/\overline{u}_{1,u}^2)$

Fig. 7 Spatial variation of thermodynamic fluctuations for the case of $M_u = 1.50$ with $M_{t,u} = 0.15$ (squares), 0.22 (circles), 0.31 (upward triangle), 0.38 (downward triangle) and $Re_{\lambda,u} = 40$: (a) shock-normal Reynolds stress; (b) transverse vorticity variance; (c) density variance; (d) pressure variance. The Reynolds stresses and the vorticity variances are normalized by their upstream mean values. The density and the pressure variances are normalized by the square of their downstream mean values and by the normalized TKE. Hollow symbols are from the data of Larsson et al. [26] and filled symbols (diamonds) are from the case of $M_u = 1.50$, $M_{t,u} = 0.15$ and $Re_{\lambda,u} = 33$ in the present simulations. The direction of arrow indicates increasing value of $M_{t,u}$. Vertical dotted lines around $k_0x_1 = 0$ denote the region of unsteady shock movement for the case from the present simulations

The effect of Taylor-scale Reynolds number on the statistics related to velocity components are discussed in detail in [26] and for the turbulent heat flux in [43]. We found similar effect for the thermodynamic variances also (not shown), where they converge to the LIA solution as the Reynolds number is increased.

We conclude this section by mentioning that the upstream turbulence used in the LIA is isotropic, purely vortical in nature with no thermodynamic fluctuations, and has the form of decaying von Kármán energy spectrum given in [25]. The turbulence database used in the numerical simulations is however little different, in the sense that the total energy is composed of 99% solenoidal fluctuations and 1% of compressible fluctuations.

3 Results and Discussion

We compare the thermodynamic variances ($\overline{\rho'^2}$, $\overline{p'^2}$, $\widetilde{T''^2}$, $\widetilde{s''^2}$) obtained from the shock-captured DNS of canonical shock-turbulence interaction with the LIA predictions. Following the Kovásznay decomposition, we first present the pure mode fluctuations, i.e., pressure and entropy variances. We next discuss the temperature and density fluctuations, which have contribution of the acoustic and the entropy modes. We normalize the density, pressure and temperature variances by the square of their respective mean downstream values ($\overline{\rho}_d^2$, $\overline{p}_d^2$, $\widetilde{T}_d^2$). The entropy variance is normalized by the square of the gas specific heat capacity at constant pressure (c_p^2). Additionally, the variances are scaled by the upstream turbulent kinetic energy divided by the square of the upstream mean shock-normal velocity ($0.5\overline{u'^2_{i,u}}/\overline{u}^2_{1,u}$). This helps to compare different cases with varying upstream turbulence intensities. It also quantifies the conversion of upstream turbulent kinetic energy, primarily in the vortical component, into thermodynamic fluctuations by the shock wave. The streamwise coordinate is normalized by the peak energy wavenumber (k_0) in the upstream field. This normalization procedure is used throughout this article, unless otherwise specified. For comparisons between the LIA and the simulation data, we use f' and f'' interchangeably in the manuscript.

3.1 Pure modes

Figure 8a presents the pressure fluctuations computed from simulations and LIA for two Mach numbers. The shocks are located at $k_0 x_1 = 0$, and the region of unsteady shock oscillations are marked by vertical lines. The pressure variance $\overline{p'^2}$ exhibits a large jump at the shock wave, followed by a rapid decay in the downstream flow. There is a mismatch between the LIA and the simulation decay rates (prominent for the higher Mach number), but the simulation far-field values are found to be comparable to those obtained from the LIA. The pressure variance obtained from the numerical simulation is higher than the LIA predictions in the range of $0^+ < k_0 x_1 < 6$. This is possibly due to non-linear effects at finite M_t, and are expected to vanish in the limit $M_t \to 0$. The pressure field is dominated by the pressure-dilatation effect, as per the budget data in Sect. 4.2, which is an inviscid mechanism. The fact that the pressure fluctuations approach a finite asymptotic value far away from the shock is entirely consistent with the notion that the shock produces a far-field radiating sound field. There are negligible pressure fluctuations in the flow upstream of the shock wave, and this is consistent with the purely vortical turbulence ($\rho_u'^{LIA} = p_u'^{LIA} = T_u'^{LIA} = s_u'^{LIA} = 0$) assumed in the linear theory.

The post-shock variation of $\overline{s'^2}$ shown in Fig. 8b is qualitatively different in the sense that it does not exhibit a rapid exponential decay as the pressure variance. There is a jump across the shock, as expected, followed by a gradual decrease in the downstream flow. The LIA predictions match the simulation values obtained immediately behind the shock, but do not reproduce the post-shock decay in the entropy variance. The interaction yields locally high values of $\overline{s'^2}$ in the shock region due to the unsteady oscillation of the shock wave. The same is true for the pressure variance in Fig. 8a. The results are similar to those presented in Ref. [42], and reproduced here with the present data for completeness.

The Kovásznay modes of entropy and acoustics are fundamentally different in terms of their evolution behind the shock wave. As per LIA, the majority of the acoustic energy decays with distance from the shock wave; in particular, those associated with the single-wave interactions exceeding the critical angle. On the other hand, the entropy mode generated at the shock propagates downstream without any change in amplitude as per the linear inviscid framework adopted by LIA. The thermodynamic field, with contribution from the acoustic and the entropy modes, exhibit a combination of these trends, as discussed subsequently.

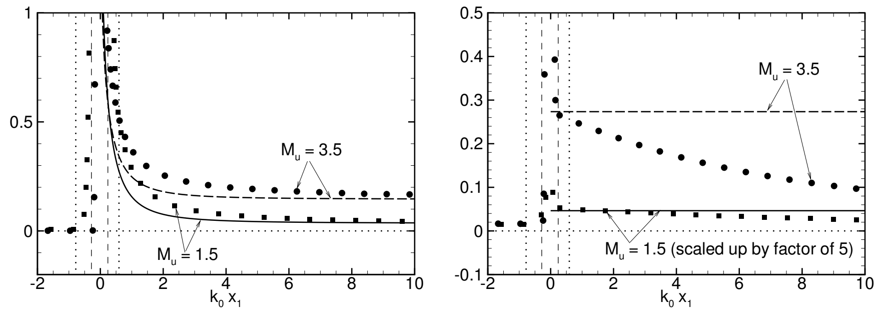

(a) $(\overline{p'^2}/\overline{p}_d^2)$ / $(0.5\overline{u'^2_{i,u}}/\overline{u}^2_{1,u})$ (b) $(\overline{s'^2}/c_p^2)$ / $(0.5\overline{u'^2_{i,u}}/\overline{u}^2_{1,u})$

Fig. 8 Spatial variation of normalized (a) pressure and (b) entropy variances for $M_u = 1.5$ (solid, squares) and 3.5 (dashed, circles). Lines represent LIA solution and symbols represent results from the present simulations. Note that the entropy variances generated by the Mach 3.5 shock wave is larger than that of the Mach 1.5 shock wave, at least by an order of magnitude; hence the data of $M = 1.5$ is scaled up by a factor of 5 to appear in the same plot. The vertical dotted and the dashed lines around $k_0x_1 = 0$ correspond to the region of unsteady shock movement for the Mach 1.5 and 3.5 cases respectively

3.1.1 Effect of M_u on the pure modes

Next we study the post-shock pressure variance as a function of shock strength in Fig. 9a. The data from the present simulations (finalized cases given in Table 1) and the cases of $M_{t,u} = 0.22$, $Re_{\lambda,u} = 40$ of [26] are compared with corresponding LIA solutions. Ideally, we would like to assess the far-field LIA predictions, but the viscous decay in the simulation data makes this difficult; we therefore perform the assessment at multiple x_1 locations between $k_0x_1 = 1$ and farther downstream. The results show a monotonic increase in $\overline{p'^2}$ with shock strength, and the simulation data, irrespective of the location, match the trend observed in the LIA predictions. In fact, the higher k_0x_1 values are closer to the LIA curves, which collapse to the asymptotic far-field solution predicted by the linear theory. There are discrepancies at lower Mach number, as well as at lower k_0x_1 (for higher Mach numbers), which are similar to those presented in

Fig. 8a. These discrepancies are attributed to the nonlinear effects due to finite M_t (see Fig. 7d).

The entropy variance plotted in Fig. 9b also shows a monotonically increasing trend with shock strength, but it seems to saturate at high Mach numbers. LIA predict a single value of $\overline{s'^2}$ for a given Mach number, whereas the entropy variance in the simulations continuously decreases with distance from the shock wave, owing to viscous effects. The far-field simulation data does not collapse, unlike the pressure variance; in fact, the decay appears to be stronger at high Mach numbers only, indicating a higher viscous effect behind stronger shocks. Comparing the $k_0x_1 = 1$ values of the entropy variance, there is excellent match between the simulation values and the LIA predictions, for the entire range of Mach numbers. The only exception is at low Mach numbers ($M = 1.23/1.27$), where the simulation data is under-predicted by the linear theory. This could possibly be a result of the small amount of entropy fluctuations in the upstream flow, which is not accounted for in the LIA predictions.

The variation of $\overline{p'^2}$ and $\overline{s'^2}$ at low Mach numbers show interesting differences. The post-shock entropy fluctuations take very low values for transonic shock waves, whereas the pressure fluctuations increase rapidly to values that are two or more orders in magnitude higher than $\overline{s'^2}$ at comparable Mach numbers. This has important consequences on the thermodynamic fluctuations, which have contributions from both the acoustic and the entropy modes. Further, the far-field pressure variance appears to saturate in the range $1.2 < M_u < 1.4$, before rising again for higher Mach numbers. Similar trends are also observed in other thermodynamic variances, as discussed subsequently.

The current numerical simulations are for an upstream turbulent Mach number of 0.15, which is lower than that in the Larsson et al. [26] cases ($M_{t,u} = 0.22$) used for comparison. The pressure and the entropy variances obtained from the current simulations are arguably closer to the LIA results, which are valid in the limit of $M_t \to 0$. See, for example, the $\overline{s'^2}$ data for $M_u = 2.5$ and 3.5, and the $\overline{p'^2}$ data for $M_u = 1.5$ and 2.5. Shock-captured DNS data at higher M_t cases, available from Ref. [26] provided in Fig. 7 show the same qualitative variation, as presented in Figs. 8 and 9. The present simulations also differ in terms of the Taylor-scale Reynolds number from the cases of Larsson et al. [26] and thus, the spatial decay in the post-shock region between the two datasets are slightly different.

Figure 10 presents the LIA near-field predictions, where the pressure variance (Fig. 10a) is the value prior to the exponential decay, and it is $2 - 5$ times larger than that at $k_0x_1 = 1$ presented in Fig. 9a, especially at low Mach numbers. The LIA pressure variance data has a non-monotonic trend with the highest value obtained at Mach 1.2, but it saturates to a finite value in the hypersonic limit. The near-field entropy variance (Fig. 10b) is identical to the far-field values, owing to the zero streamwise variation in $\overline{s'^2}$ as predicted by LIA.

As noted earlier, it is difficult to obtain the near-field variances using conventional (fixed point) averaging of the simulation data. The high values of the thermodynamic fluctuations computed in the region of the shock wave are largely due to the unsteady shock oscillation. On the other hand, the statistics computed at the edge of the mean shock thickness is strongly affected by the rapid exponential decay, at least for the

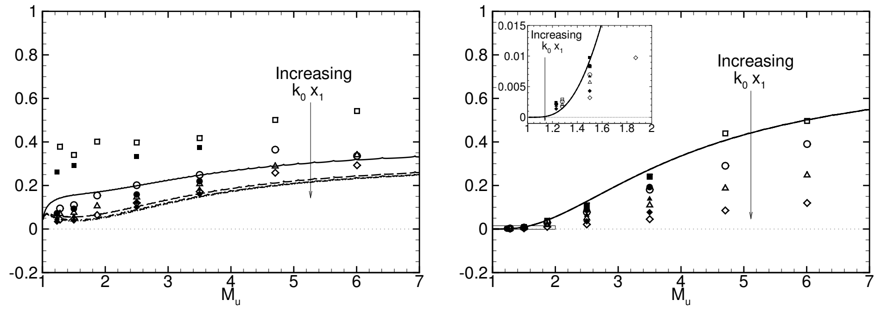

(a) $(\overline{p'^2}/\overline{p}_d^2)\ /\ (0.5\overline{u'^2_{i,u}}/\overline{u}^2_{1,u})$ (b) $(\overline{s'^2}/c_p^2)\ /\ (0.5\overline{u'^2_{i,u}}/\overline{u}^2_{1,u})$

Fig. 9 Variation of normalized (a) pressure and (b) entropy variances at four different downstream locations from LIA (lines) and simulations (symbols): $k_0 x_1 = 1$ (solid, squares), 3 (dashed, circles), 6 (dash-dotted, triangles), 12 (dash-double dotted, diamonds). Open symbols are from Larsson et al. [26] data for the cases of $M_{t,u} = 0.22$, $Re_{\lambda,u} = 40$ and filled symbols are from present simulations (given in Table 1).

pressure variance. By comparison, the threshold method computes statistics based on the data at the edge of the instantaneous shock. It follows the idea of near-field LIA solution closely, and captures the fluctuation levels that are largely unaffected by the post-shock variations. It is found that the pressure and the entropy variances obtained using the threshold method match the LIA results closely. Note that the simulation data corresponds to the STI cases computed in the current work, as the instantaneous shock data is not available from the earlier scDNS cases of [26].

Ref. [42] present the pressure and the entropy variances for the different Mach number cases of [26]. The near-field data in Ref. [42] is obtained by extrapolating the post-shock value back to the shock center. The procedure is prone to error, because of the large gradients in the pressure variance behind the shock wave. This is especially true at low Mach numbers, as noted in [42], with large region of unsteady shock oscillations, and this precludes accurate computation of the near field statistics from the simulation data. The threshold method, on the other hand, gives more reliable near-field data from the scDNS solution and they show excellent match with LIA result for a wide range of Mach numbers.

To show the effectiveness of the threshold method, the results obtained from the sequence of grids provided in Table 1 are also presented in Fig. 10. The threshold method is highly sensitive to the shock-normal grid spacing due to the inherent use of dilatation as the threshold quantity. The largest error in the statistics between two consecutive finer grid spacings in the shock-normal direction for the same transverse grid spacing is found to be slightly less than 10%. The statistics obtained using the threshold method, though having a relatively large error, are found to be close to the LIA near-field values presented.

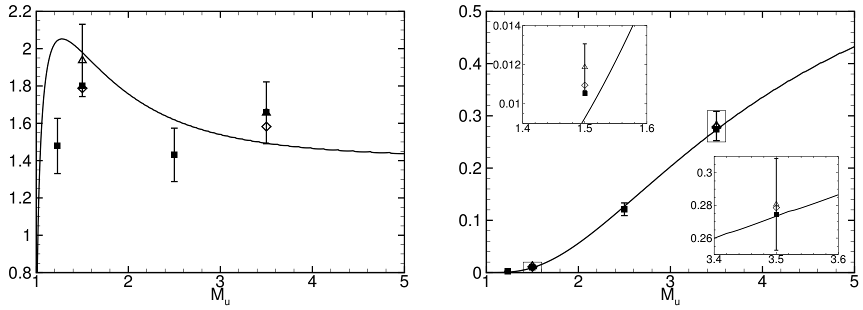

(a) $(\overline{p'^2}/\overline{p}_d^2)\ /\ (0.5\overline{u'^2_{i,u}}/\overline{u}^2_{1,u})$ (b) $(\overline{s'^2}/c_p^2)\ /\ (0.5\overline{u'^2_{i,u}}/\overline{u}^2_{1,u})$

Fig. 10 Variation of normalized (a) pressure and (b) entropy variances at $k_0x_1 = 0^+$ (in LIA) and the instantaneous shock location (in simulations) obtained using the threshold method. Lines represent LIA solution and symbols represent simulation values. The symbols are 1.23, 1.5*c*, 2.5, 3.5*c* (squares) ; 1.5*d*, 3.5*d* (triangles) ; 1.5*e*, 3.5*e* (diamonds). The error bars denote the +/ − 10% error that we estimated in Sect. 2.1.3

3.2 Temperature fluctuations

The temperature variance shown in Fig. 11a is similar to $\overline{p'^2}$ (Fig. 8a), with high values across the shock that decay rapidly in the downstream flow. Additionally, the temperature fluctuations exhibit a slower but steady decrease farther away from the shock wave ($k_0x_1 > 2$). This is more prominent in the higher Mach number case, and is akin to the decay of entropy fluctuations observed earlier. Shock-captured DNS data presented in Refs. [12, 13] show similar trends. On the other hand, the temperature variance reaches an asymptotic far-field value in the LIA solution.

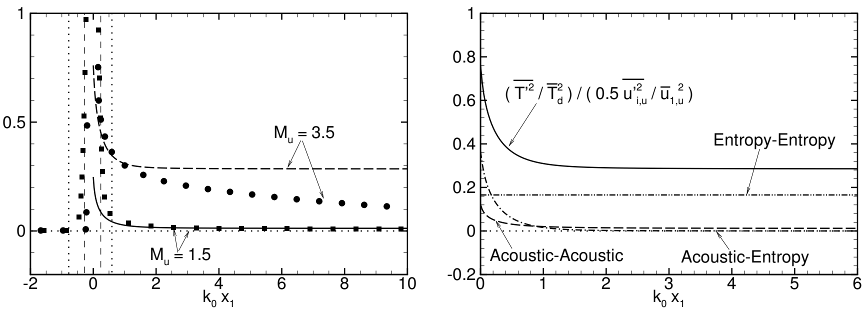

(a) Spatial variation of $(\overline{T'^2}/\overline{T}_d^2)\ /\ (0.5\overline{u'^2_{i,u}}/\overline{u}^2_{1,u})$ (b) Kovásznay mode components for $M_u = 3.5$

Fig. 11 Spatial variation of normalized temperature variance $(\overline{T'^2}/\overline{T}_d^2)\ /\ (0.5\overline{u'^2_{i,u}}/\overline{u}^2_{1,u})$ (a) for $M_u = 1.5$ (solid, squares) and 3.5 (dashed, circles) with lines representing LIA solution and symbols representing current simulations; (b) components of the variance obtained by the Kovásznay type mode decomposition for $M_u = 3.5$ case.

The spatial variation of the temperature variance is explained in terms of the Kovásznay modes for the Mach 3.5 case in Fig. 11b. The results are qualitatively similar to that for Mach 1.5 in Ref. [42], except for the large entropy component at the higher Mach number. The far-field $\overline{T'^2}$ is almost entirely given by the *ee*-component, which is invariant in k_0x_1 as per the inviscid analysis. The post-shock rapid decay in $\overline{T'^2}$ is due to the *aa*- and *ae*-components, both related to the acoustic mode generated at the shock wave. All the components are positive for the temperature fluctuations, giving a large value at the shock and they together give a monotonic decay of $\overline{T'^2}$ to its far-field value due to the decrease in the acoustic components along the shock-normal direction.

A comparison of the temperature fluctuations computed at different streamwise locations in Fig. 12a shows an M_u^2 increase with shock strength, except for a small range of non-monotonic variation near Mach 1.2. The LIA results are qualitatively similar to the pressure variance, with the different k_0x_1 curves collapsing to the far-field value of $\overline{T'^2}$. The simulation data, by comparison, exhibits the steady decrease with k_0x_1, akin to the entropy variance plotted in Fig. 9b, especially at high Mach numbers. In spite of the scatter, the data points follows the trend in the LIA curves well, for the entire range of Mach numbers.

The simulation statistics computed using the threshold method (Fig. 12b) shows a much better match with the near-field LIA predictions. The values are, once again, higher by about an order in magnitude compared to the far-field $\overline{T'^2}$ at a given Mach number. The simulation data points are limited to Mach 3.5, corresponding to the current simulations, and it is lower than the LIA results.

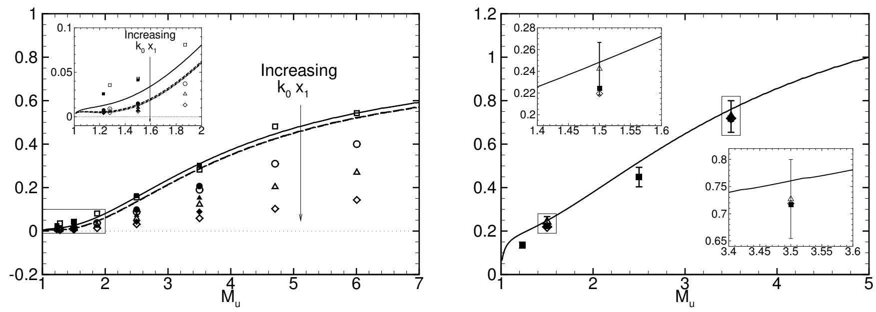

(a) $k_0x_1 = 1, 3, 6, 12$ (b) $k_0x_1 = 0^+$

Fig. 12 Variation of normalized temperature variance $(\overline{T'^2}/\overline{T}_d^2)$ / $(0.5\overline{u'^2_{i,u}}/\overline{u}^2_{1,u})$ at various streamwise locations (a) : $k_0x_1 = 1$ (solid, squares), 3 (dashed, circles), 6 (dash-dotted, triangles), 12 (dash-double dotted, diamonds) locations where, lines represent LIA solution and symbols correspond to simulations as given in figure 9, and at (b) $k_0x_1 = 0^+$ (near-field) location where the downstream statistics from the simulation data were collected at the instantaneous shock location using the threshold method. The line and symbol types, and the error bar values are as mentioned in the caption of Fig. 10

Figure 13 presents the Kovásznay mode decomposition of the LIA temperature variance and is plotted as a function of the shock Mach number. The far-field data (in

Fig. 13b) shows that the temperature fluctuations at high Mach number are entirely due to the entropy mode, whereas the acoustic mode is dominant in the transonic range. This is similar to the observation in Ref. [42] in terms of the percentage contribution of each component to the temperature variance. Interestingly, the data presented here shows that the non-monotonic behavior of far-field $\overline{T'^2}$ with Mach number is caused by the switch (around $M_u = 1.4$) between the acoustic and the entropy contributions to the temperature field. The near-field data (in Fig. 13a) has a similar trend, except for a large contribution from the correlation between the acoustic and the entropy modes for $M_u > 2$. The ae-component dies down quickly, and has a vanishing magnitude in the far-field, owing to the different wave speeds of the acoustic and non-acoustic modes. For the propagating acoustic waves, the integration of the ae-correlation term can be shown to algebraically decay with x_1 [35, 11].

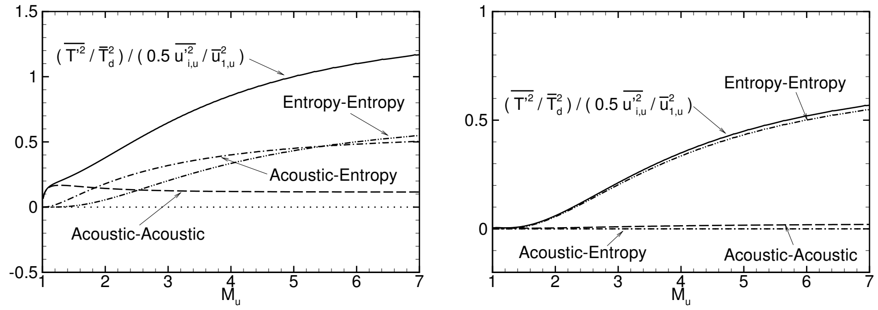

(a) $k_0 x_1 = 0^+$ (b) $k_0 x_1 = 2\pi$

Fig. 13 Variation against shock-strength for the Kovásznay components in normalized temperature variance $(\overline{T'^2}/\overline{T}^2_d)$ / $(0.5\overline{u'^2_{i,u}}/\overline{u}^2_{1,u})$ taken from the locations (a) $k_0 x_1 = 0^+$ and (b) $k_0 x_1 = 2\pi$

3.3 Density fluctuations

The density variances plotted in Fig. 14 exhibit different qualitative variation at Mach 1.5 and 3.5. At the lower Mach number, it attains relatively high values across the shock, followed by a rapid decay in the downstream flow, similar to pressure and temperature variances presented earlier. LIA results, once again, compare well with the scDNS data, similar to pressure and temperature variances presented earlier.

At the higher Mach number, the simulation density variance has a non-monotonic variation behind the shock, with a peak value around $k_0 x_1 = 1$. The trend is similar to that of the shock-normal Reynolds stresses [30, 36, 27, 26] and the turbulent energy flux [43], and is also observed in LIA. The LIA gives low density fluctuations in the near-field ($k_0 x_1 = 0^+$) and it increases rapidly to high far-field values. As earlier, the linear theory results reach an asymptotic finite $\overline{\rho'^2}$ far away from the shock, whereas

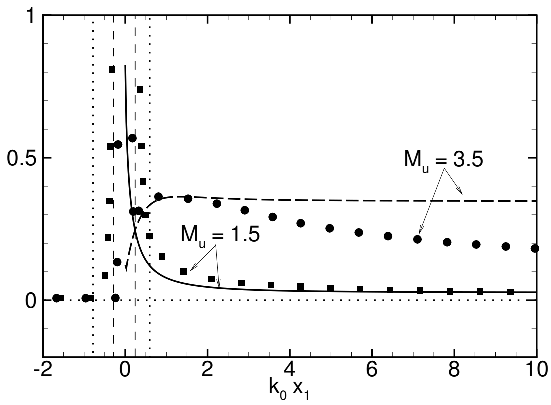

Fig. 14 Spatial variation of normalized density variance $(\overline{\rho'^2}/\overline{\rho}_d^2)$ / $(0.5\overline{u'^2_{i,u}}/\overline{u}^2_{1,u})$ for M_u = 1.5 (solid, squares) and 3.5 (dashed, circles) with lines representing LIA solution and symbols for current numerical simulation results

the simulation data shows a steady viscous decay downstream of the local peak behind the shock wave.

We use Kovásznay mode decomposition of the density variance (Fig. 15) to explain the non-monotonic behavior observed behind strong shocks. As expected the acoustic components have an exponential variation with x_1, while the entropy component is constant in the downstream flow. The aa- and ee-components are positive, while the correlation between the acoustic and the entropy modes has a negative contribution to the density variance. In the acoustic-adjustment region ($0 < k_0x_1 < 2$), the balance between all the three components determine the behavior of $\overline{\rho'^2}$. At low Mach numbers, the variation of $\overline{\rho'^2}$ in the post-shock field follows a monotonic decay due to the small magnitude of the ae-component. By comparison, the large negative ae-contribution to $\overline{\rho'^2}$ at Mach 3.5 counters the positive pure-acoustic component resulting in a non-monotonic variation behind the shock wave. This, along with the viscous decay in the far-field, results in the local peak in the density variance observed in the Mach 3.5 simulation data plotted in Fig. 14.

3.3.1 Effect of shock strength on the density fluctuations

Figure 16a plots the variation of density fluctuations with Mach number at different locations downstream of the shock. All the LIA curves converge to the far-field $\overline{\rho'^2}$ values, except for minor variations at low Mach numbers. As expected, the density variance increases with shock strength, but saturates in the limit of $M_u \rightarrow \infty$. This is unlike temperature and pressure fluctuations presented earlier, which follow an M_u^2 scaling in the hypersonic range. Interestingly, LIA predicts that the post-shock fluctuations in pressure, density and temperature scale with their respective post-shock mean values. For a fixed upstream thermodynamic state, the mean pressure and temperature continue to increase at high Mach numbers, and the same is true for the

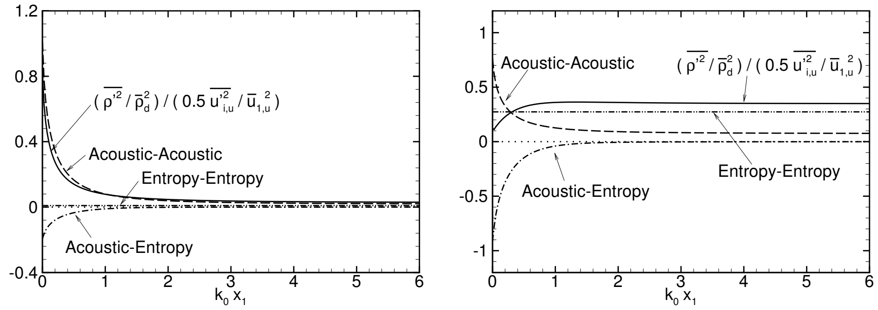

(a) $M_u = 1.5$ (b) $M_u = 3.5$

Fig. 15 Spatial variation of normalized density variance $(\overline{\rho'^2}/\overline{\rho}_d^2)$ / $(0.5\overline{u'^2_{i,u}}/\overline{u}^2_{1,u})$ components obtained by a Kovásznay type mode decomposition for (a) $M_u = 1.5$ and (b) $M_u = 3.5$

corresponding fluctuations. By comparison, a finite asymptotic density jump in the hypersonic limit results in a finite $\rho'/\overline{\rho}$ as $M_u \to \infty$.

The simulation data points at the different spatial locations follow the LIA trend with increasing Mach number. The variations are similar to that of the temperature fluctuations shown in Fig. 12a, such that the LIA values are lower than simulations for locations closer to the shock, and are larger than the simulation values further downstream. Once again, the scatter in the simulation data is due to viscous effects, which appear to increase with Mach number as the magnitude of the post-shock density variance increases. The almost uniform decrease in $\overline{\rho'^2}$ values for high shock strengths indicates that the decay is similar to the decay due to viscous effects and increase linearly with k_0x_1.

Kovásznay mode decomposition for the far-field density variance is plotted as a function of the shock Mach number in Fig. 16b. The data corresponds to $k_0x_1 = 2\pi$ and there are minimal changes beyond this value. Both the entropy and the acoustic contributions increase with Mach number, with a large *ee*-component in the high Mach number interactions and the *aa*-component dominating at low Mach numbers. The *ae*-contribution to the far-field density variance is vanishingly small, as the correlation between the acoustic and the entropy modes decay away from the shock wave. A small plateau is visible in the lower Mach number range, and it is characteristic of the acoustic mode (in Fig. 9a). The switch between the dominant *aa*-component to the large *ee*-component occurs near Mach 1.6, resulting in a further rise in $\overline{\rho'^2}$ with Mach number.

The LIA near-field density variance (Fig. 17a) show a unique variation with Mach number. It increases to attain a peak value for Mach 1.2 and then decreases at higher Mach number. As per the Kovásznay mode decomposition in Fig. 17b, this non-monotonic variation is caused by a rapid increase in the magnitude of the *ae*-component at higher Mach numbers. It is found that the acoustic and the entropy components of the density field are out-of-phase with each other. A large negative *ae*-component cancels the positive *aa*- and *ee*-contributions to result in vanishingly small

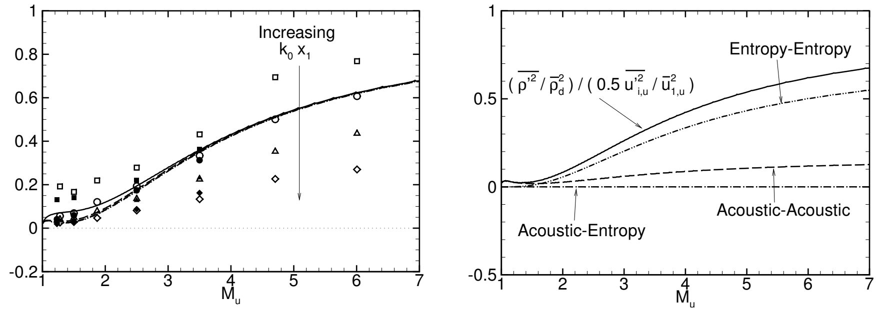

(a) Effect of shock strength at $k_0x_1 = 1,\ 3,\ 6,\ 12$ (b) Kovásznay mode components at $k_0x_1 = 2\pi$

Fig. 16 Variation of normalized density variance $(\overline{\rho'^2}/\overline{\rho}_d^2)\,/\,(0.5\overline{u_{i,u}'^2}/\overline{u}_{1,u}^2)$ against upstream Mach number at (a) the $k_0x_1 = 1$ (solid, squares), 3 (dashed, circles), 6 (dash-dotted, triangles), 12 (dash-double dotted, diamonds) locations. Lines represent LIA solution and symbols correspond to the simulations as given in figure 9, (b) Kovásznay mode components of the density variance at the far-field region ($k_0x_1 = 2\pi$)

near-field density fluctuations in the limit of infinite shock Mach number. The density statistics computed using the threshold method also shows a similar non-monotonic trend with Mach number. The values computed at Mach 1.5 and 2.5 are comparable to the LIA results. On the other hand, the threshold method under-predicts the near-field density variance at the weakest interaction case (Mach 1.23) and over-predicts the LIA value for Mach 3.5. The reason for these discrepancies is not known.

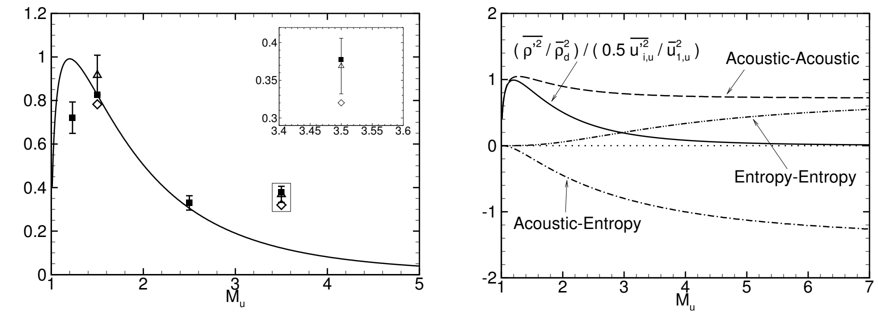

(a) Effect of shock strength at $k_0x_1 = 0^+$ (b) Kovásznay mode components at $k_0x_1 = 0^+$

Fig. 17 Variation of normalized density variance $(\overline{\rho'^2}/\overline{\rho}_d^2)\,/\,(0.5\overline{u_{i,u}'^2}/\overline{u}_{1,u}^2)$ against upstream Mach number at (a) $k_0x_1 = 0^+$ location where the downstream statistics from the simulation data (symbols) were collected at the instantaneous shock location using the threshold method. The line and symbol types, and the error bar values are as mentioned in the caption of Fig. 10. (b) Kovásznay mode components of the density variance at the near-field region ($k_0x_1 = 0^+$)

We conclude this section by emphasizing that the shock generates thermodynamic fluctuations even in the absence of thermodynamics in the upstream turbulent field.

The post-shock field is found to be isentropic only for weak shock strengths ($M_u \lessapprox 1.7$) by comparing the polytropic exponents relating the density, pressure and temperature fluctuations via the isentropic relation, which was also shown in [30]. These results apply to vortical turbulence upstream of the shock wave, and not for inflow turbulence with considerable amount of entropy and acoustic fluctuations ($\geq 50\%$) as considered in [35, 14, 37, 36, 20].

4 Budgets of thermodynamic fluctuations

The different post-shock behavior exhibited by the different thermodynamic variances for varying Mach numbers is explored further in terms of their transport equation. Shock-captured DNS data is used to compute the budget of the source terms, so as to identify the dominant physical mechanisms responsible for a particular post-shock behavior. Note that the transport equations presented in this section are for steady one-dimensional mean flow encountered in canonical shock-turbulence interaction. A more detailed description of the transport equations for the thermodynamic variances can be found in [10].

4.1 Density variance

The transport equation for density variance ($\overline{\rho'^2}$) can be obtained by multiplying ρ' to the continuity equation and taking the respective averages. For canonical shock-turbulence interaction with a steady mean shock ($\partial_t = 0$) and one-dimensional mean flow, the averages are functions of the shock-normal direction x_1 only and $\partial_{x_2}\overline{f} = \partial_{x_3}\overline{f} = 0$, where ∂_{x_2} and ∂_{x_3} corresponds to derivatives in shock-parallel directions. The transport equation thus reduces to,

$$\begin{aligned}\underbrace{\partial_{x_1}(\widetilde{u}_1\overline{\rho'^2})}_{\text{Convection}} = & \underbrace{-\partial_{x_1}(\overline{\rho'^2 u_1''})}_{\text{Diffusion}} \underbrace{-2\overline{\rho'^2}\partial_{x_1}\widetilde{u}_1 - 2\overline{\rho' u_1''}\partial_{x_1}\overline{\rho}}_{\text{Production}} \\ & \underbrace{-2\overline{\rho}\,\overline{\rho'\partial_{x_j}u_j''} - \overline{\rho'^2\partial_{x_j}u_j''}}_{\text{Dilatation}},\end{aligned} \tag{2}$$

where ∂_{x_1} indicates derivatives taken in the shock-normal direction.

Figure 18 shows the budget of the terms in the transport equation for density variance for the four scDNS cases computed as part of the current work. The term on the LHS of Eq. (2) is the convection term, which is the transport of density variance by the mean velocity field. The convection term is usually negative and for the sake of easy comparison, the negative of the convection term is shown in the figure. The last two terms represent dilatation effect on density fluctuations, with the second term being of higher order, and hence has negligible contribution. The first dilatation term is the primary source term in the post-shock evolution of density variance, and is comparable to the convection term. This is similar to that reported by [14] for a Mach 2 shock-turbulence interaction. In the absence of a strong mean compression outside the region of unsteady shock motion (shown by the vertical dotted lines near to

$k_0x_1 = 0$), the fluctuating dilatation is the main contributor to the source terms as well as the overall budget. The density-dilatation correlation is positive for the first three cases resulting in a negative source term. It monotonically decreases in magnitude with increasing distance from the shock wave with a small exception for $k_0x_1 < 1$ in the $M_u = 2.5$ case. For the Mach 3.5 interaction, the convection and dilatation terms have a non-monotonic variation, similar to the spatial variation of the density variance in this case. The budget terms change sign behind the shock wave, and the zero crossing corresponds to the peak in the density variance observed in Fig. 14.

The diffusion term (first term on the right-hand side) represents the turbulent transport of density fluctuations in the post-shock flow. It is of an order higher than the convection term and is expected to have a small contribution. The production term generates density fluctuations through the gradient of mean quantities (density and velocity). Larsson and Lele [27] report small variation in the mean velocity and density in the region immediately behind the shock. This is due to the fact that the jump conditions across a shock wave are slightly different for a turbulent flow than the standard RH conditions for flows without fluctuations [32]. Small variation in mean quantities behind the shock results in a finite gradient in the shock-normal direction, which in turn results in a non-zero production term behind the shock wave. The inset in each sub-figure of Fig. 18 shows a highly magnified view of the region immediately behind the shock, where the diffusion and production terms have non-negligible contribution. The diffusion and the production terms are indeed smaller than the dominant terms by at least an order of magnitude. The error computed as the sum of all the terms in the transport equation (with the convection term placed on the RHS) is also found to be small.

4.2 Pressure variance

The transport equation for pressure variance ($\overline{p'^2}$) is obtained by taking a moment of the pressure transport equation with p'. The transport equation for instantaneous pressure can be obtained from the energy conservation equation using the relation $p = (\gamma - 1)\rho e^i$, where $e^i = c_v T$ is the internal energy and c_v is the gas specific heat capacity at constant volume. The simplified version of the pressure variance transport equation for the canonical shock-turbulence interaction is given by,

$$
\begin{aligned}
\underbrace{\partial_{x_1}(\widetilde{u}_1\overline{p'^2})}_{\text{Convection}} = & \underbrace{-\partial_{x_1}(\overline{p'^2u_1''}) + 2(\gamma-1)[\partial_{x_1}(\overline{p'q_1})]}_{\text{Diffusion}} \\
& \underbrace{-2\overline{p'u_1''}\partial_{x_1}\overline{p} - 2(\gamma-1)\overline{p'^2}\partial_{x_1}\widetilde{u}_1 + 2(\gamma-1)\overline{p'\sigma_{i1}}\,\partial_{x_1}\widetilde{u}_i}_{\text{Production}} \\
& \underbrace{-2\gamma\overline{p}\overline{p'\partial_{x_j}u_j''} - (2\gamma-1)\overline{p'^2\partial_{x_j}u_j''}}_{\text{Dilatation}} \\
& \underbrace{-2(\gamma-1)\overline{q_j\,\partial_{x_j}p'}}_{\text{Dissipation}} + \underbrace{2(\gamma-1)\overline{p'\sigma_{ij}\,\partial_{x_j}u_i''}}_{\text{Triple correlations}},
\end{aligned}
\tag{3}
$$

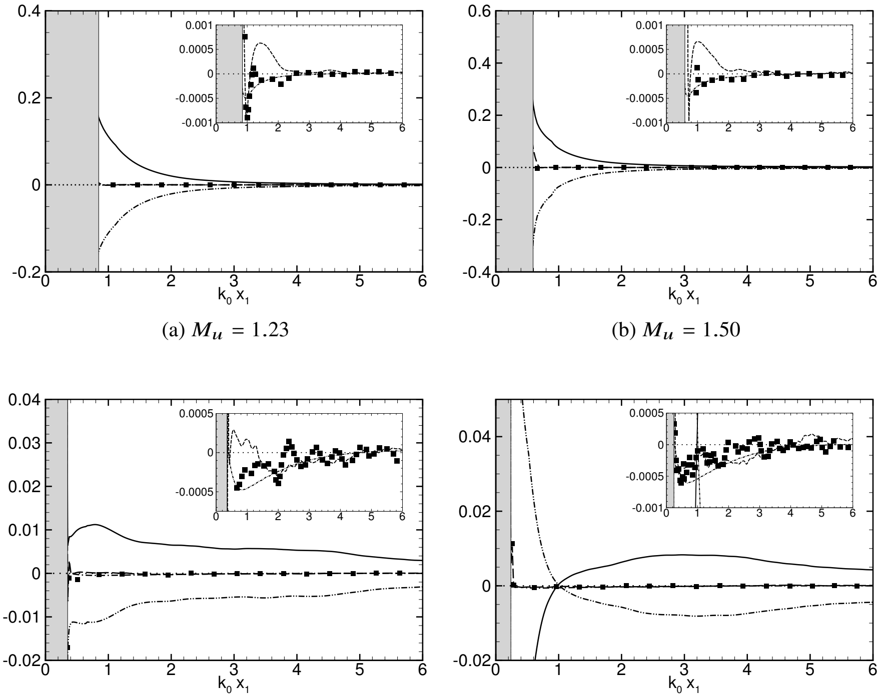

(a) M_u = 1.23 (b) M_u = 1.50

(c) M_u = 2.50 (d) M_u = 3.50

Fig. 18 Budgets of terms in the transport equation of $\overline{\rho'^2}$ for different Mach numbers: (a) $M_u = 1.23$, (b) $M_u = 1.50$, (c) $M_u = 2.50$ and (d) $M_u = 3.50$ from the present simulations. Convection is shown by solid lines, diffusion by dashed lines, production by dash-dotted lines, dilatation by dash-double dotted lines, and the sum of all terms are shown by square symbols. The density variances are normalized as mentioned in Sect. 3, i.e., by the square of downstream mean density ($\overline{\rho}_d^2$) and the normalized upstream turbulent kinetic energy ($0.5\,\overline{u'^2_{i,u}}/\overline{u}^2_{1,u}$). The derivative operator is normalized by the peak energy wavenumber (k_0) and the upstream mean shock-normal velocity ($\overline{u}_{1,u}$), whereas the streamwise direction is normalized by the peak energy wavenumber. Region of unsteady shock motion is shown by a grey band. Inset shows the contribution of the production and the diffusion terms which are at least an order of magnitude lesser than the dominant terms

The transport equation for pressure variance has a form similar to that of the density variance presented above, with terms representing mean convection, diffusion, production and dilatation. In addition, there is dissipation effect and a triple correlation including viscous stresses. The dissipation term consists of the product of the gradients in fluctuating pressure and temperature with the conductivity of the fluid, whereas the triple correlation can be interpreted as a correlation of the pressure fluctuations with the viscous work that contributes to the energy of the fluid element. Both the viscous correlation and the dissipation terms are found to be negligible in the $\overline{p'^2}$ budgets computed using the current simulation data. On the other hand, the pressure dilatation correlation term is the main contributor to the budget, and it is about two orders in magnitude larger than the other source terms. The first part balances the convection term, as in the $\overline{\rho'^2}$ budget, while the second part of the dilatation term consists of higher order correlation, and is found to be comparatively small. Unlike earlier, the pressure-dilatation term is always negative, and it exponentially decreases with distance from the shock wave - a trend similar to $\overline{p'^2}$ at all Mach numbers.

The production of pressure fluctuation due to mean pressure gradient depends on the pressure-velocity correlation. A second production term is given by the mean velocity gradient in the streamwise direction. These are, once again, found to be negligible, owing to the small magnitude of the post-shock mean field variation. Diffusion of pressure fluctuations are due to the turbulent transport of pressure fluctuations by the velocity field, as well as a correlation of the fluctuating pressure with the conduction heat flux. Both the diffusion terms are much smaller than the dominant dilatation effect, and this is similar to the density budget presented in Fig. 18.

Figure 19 plots the mean convection and the dilatation source term for varying Mach numbers. All the curves are qualitatively similar, and there is a clear trend of an decrease in magnitude with increasing Mach number. The data is normalized by the upstream turbulent kinetic energy, where the mean shock-normal velocity is normalized by its upstream mean value and the thermodynamic fluctuations are normalized by their respective mean values downstream of the shock wave.

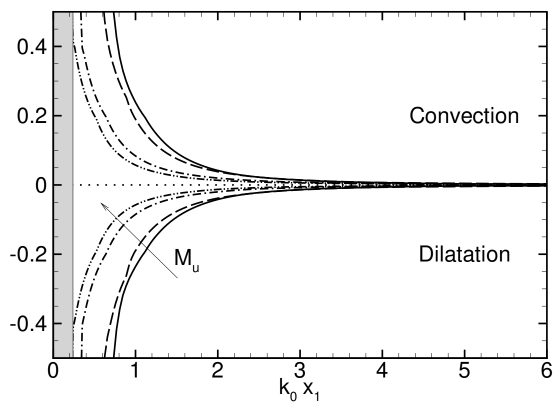

Fig. 19 Budgets of terms in the transport equation of $\overline{p'^2}$ for different Mach numbers: $M_u = 1.23$ (solid), $M_u = 1.50$ (dashed), $M_u = 2.50$ (dash-dotted), $M_u = 3.50$ (dash-double dotted) from the current simulations. The pressure variances are normalized as mentioned in Sect. 3 and the derivative operator is normalized by the factor $k_0\overline{u}_{1,u}$. Convection terms are represented on the positive axis and the dilatation terms are shown at the negative axis. Region of unsteady shock motion for $M_u = 3.50$ (thinnest shock) case is shown by the grey band. Production, diffusion, dissipation and triple correlation terms (not shown) are very small in magnitude compared to the dominant terms

4.3 Temperature variance

We follow the Favre averaging procedure for temperature and thus, the temperature variance transport equation, given in Eq. (4) is obtained by multiplying $\rho T''$ with the transport equation for temperature, followed by Reynolds averaging. The transport equation for temperature is obtained from the internal energy component of the total energy conservation equation and can also be obtained once the pressure transport equation is known. The transport equation written for our model problem is given in Eq. (4).

$$\begin{aligned}
\underbrace{\partial_{x_1}(\widetilde{u}_1\overline{\rho T''^2})}_{\text{Convection}} = & \underbrace{-\partial_{x_1}(\overline{\rho T''^2 u_1''}) + (2/c_v)\partial_{x_1}(\overline{T'' q_1})}_{\text{Diffusion}} \\
& \underbrace{-2\overline{\rho T'' u_1''}\partial_{x_1}\widetilde{T} - (\overline{p}\overline{T''} + \overline{p' T''})\partial_{x_1}\widetilde{u}_1 + (2/c_v)\overline{T''\sigma_{i1}}\,\partial_{x_1}\widetilde{u}_i}_{\text{Production}} \\
& \underbrace{-(2/c_v)\overline{p}\overline{T''\partial_{x_j}u_j''} - (2/c_v)\overline{p' T''\partial_{x_j}u_j''}}_{\text{Dilatation}} \\
& \underbrace{-(2/c_v)\overline{q_j\,\partial_{x_j}T''}}_{\text{Dissipation}} + \underbrace{(2/c_v)\overline{T''\sigma_{ij}\partial_{x_j}u_i''}}_{\text{Triple correlations}},
\end{aligned} \tag{4}$$

where $c_v = R/(\gamma - 1)$ and R is the specific gas constant.

The above equation matches term-by-term to the pressure variance equation. There are minor differences in terms of p' replaced by ρT" and c_v in place of the factors of γ in Eq. (3). The budget of temperature variance is once again dominated by the acoustic effect, with a large dilatation source term balancing the convection term behind the shock wave (see Fig. 20). The main difference is the dissipation term at higher Mach number. The dilatation effect decays rapidly to take very small values away from the shock, while the dissipation term shows a slow decrease in magnitude. So, the viscous dissipation of temperature fluctuations takes over the inviscid dilatation effect at some distance away from the shock wave. The location of this change moves closer to the shock with increasing shock strength as the dissipation becomes more negative with increasing Mach number. Farther away from the shock, the budget is dominated by the negative dissipation term, which balances the dilatation and convection effects. Interestingly, the dilatation source term changes sign to become positive for $k_0 x_1 > 1$. This is true for all Mach numbers, and is not seen in the pressure and density budget plots, except for Mach 3.5 density budget, where the change in sign is associated with a local peak in the density variance downstream of the shock. The temperature variance has no such local peak in magnitude, and it is governed primarily by the viscous dissipation at large distances from the shock wave.

4.4 Entropy variance

Using the fundamental thermodynamic relation, specifically the form of Gibbs relation: $T ds = de - (p/\rho^2)d\rho$, the transport equation for entropy (s) can be obtained from the internal energy equation. The transport equation for its variance is obtained by taking a moment with $\rho s''$ similar to the procedure followed for temperature variance given in Eq. (4). For the case of canonical shock-turbulence interaction, the transport

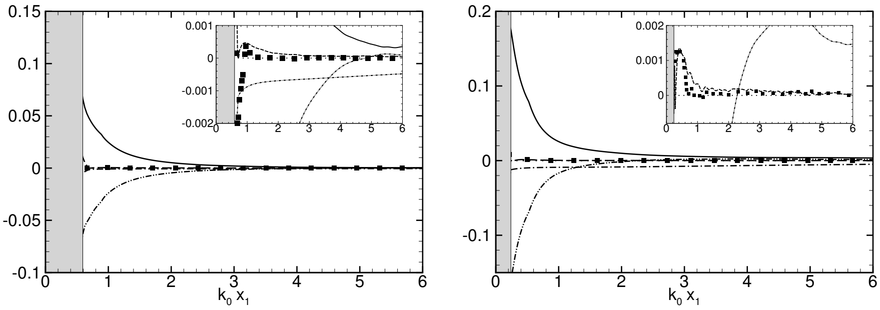

(a) $M_u = 1.50$ (b) $M_u = 3.50$

Fig. 20 Budgets of terms in the transport equation of $\overline{\rho T''^2}$ for two Mach numbers: (a) $M_u = 1.50$ and (b) 3.50 from the present simulations. Convection (solid), dissipation (dash-dotted), dilatation (dash-double dotted), and the sum of all terms (square symbols). Sum of production, diffusion, and triple correlation terms are shown by dashed lines, and are very small in magnitude compared to the dominant terms. The temperature variances are normalized as mentioned in Sect. 3 and other normalization details follow as given in the caption of Fig. 18. Region of unsteady shock motion is shown by the grey band

equation is written as,

$$
\begin{aligned}
\underbrace{\partial_{x_1}(\widetilde{u}_1\overline{\rho s''^2})}_{\text{Convection}} = & \underbrace{-\partial_{x_1}(\overline{\rho s''^2 u_1''}) + 2\partial_{x_1}\left(\overline{\frac{q_1}{T}s''}\right)}_{\text{Diffusion}} \\
& \underbrace{-2\overline{\rho s'' u_1''}\partial_{x_1}\widetilde{s} + 2\overline{\frac{\sigma_{i1}}{T}s''}\partial_{x_1}\widetilde{u}_i + 2\overline{\frac{q_1}{T}\frac{s''}{T}}\partial_{x_1}\widetilde{T}}_{\text{Production}} \\
& \underbrace{-2\overline{\frac{q_j}{T}\partial_{x_j}s''}}_{\text{Dissipation}} + \underbrace{2\overline{\frac{\sigma_{ij}}{T}s''\partial_{x_j}u_i''} + 2\overline{\frac{q_j}{T}\frac{s''}{T}\partial_{x_j}T''}}_{\text{Triple correlations}}.
\end{aligned}
\tag{5}
$$

The entropy variance transport equation and its budget plots in Fig. 21 are very different from those for the other thermodynamic fluctuations. The entropy budget is entirely governed by viscous dissipation term, which includes a product of fluctuating heat flux vector and entropy gradients in the fluid. There is a slow monotonic decay in the dissipation rate and the steep gradient in the vicinity of the shock wave is due to unsteady shock oscillations. The triple correlation term has a non-negligible contribution to the overall budget, especially at low Mach numbers. It has the usual correlation of the viscous work with the entropy fluctuations. There is an additional term consisting of the viscous dissipation of temperature fluctuations and the fluctuating entropy.

The dissipation effect balances the positive convection and small values of triple correlations for weaker interactions. The magnitude of viscous dissipation increases with Mach number. A similar increase in the dissipation of temperature fluctuations is reported in Fig. 20. We note that the entropy being a pure mode, has no contribution from the acoustic waves generated at the shock. This is evident from the absence of the dilatation effect in the $\widetilde{s''^2}$ transport equation. We also identify that the diffusion term has the same form as earlier, and is negligible except for the immediate vicinity of the shock wave. Production due to the post-shock gradients in mean entropy, mean temperature and mean velocity is also small and comparable to the error in the budget.

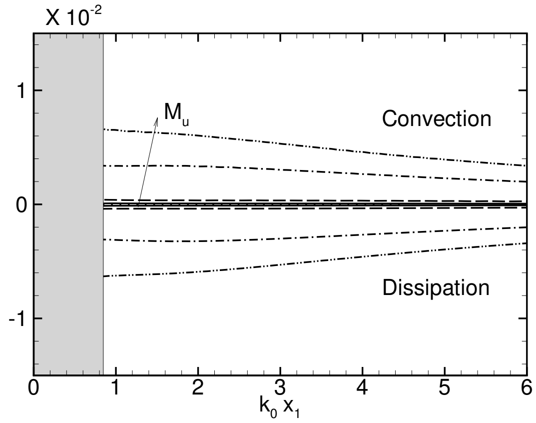

Fig. 21 Budgets of terms in the transport equation of $\overline{\rho s''^2}$ for different Mach numbers: $M_u = 1.23$ (solid), $M_u = 1.50$ (dashed), $M_u = 2.50$ (dash-dotted), $M_u = 3.50$ (dash-double dotted) from the current simulations. The entropy variances are normalized as mentioned in Sect. 3 and other normalization details follow as given in the caption of Fig. 18. Convection terms are represented on the positive axis and the dissipation terms are shown at the negative axis. Region of unsteady shock motion for $M_u = 1.23$ (thickest shock) case is shown by the grey band. Production, diffusion and triple correlation terms (not shown) are very small in magnitude in comparison to the dominant terms

5 Modeling implications

We identify that the transport of the thermodynamic variances in the post-shock region to be dominated by dilatational effects and dissipative mechanisms (see Sect. 4). The transport equations can be approximated to a suitable degree in the form of,

$$\widetilde{u}\partial_{x_1}\overline{\rho'^2} \approx -2\overline{\rho}\,\overline{\rho'\partial_{x_j}u_j''}, \tag{6}$$

$$\widetilde{u}\partial_{x_1}\overline{p'^2} \approx -2\gamma\overline{p}\,\overline{p'\partial_{x_j}u_j''}, \tag{7}$$

$$\widetilde{u}\partial_{x_1}\widetilde{T''^2} \approx -(2/c_v)\overline{p}\,\overline{T''\partial_{x_j}u_j''} - (2/c_v)\overline{q_j\partial_{x_j}T''}, \tag{8}$$

$$\widetilde{u}\partial_{x_1}\widetilde{s''^2} \approx -2\overline{(q_j/T)\partial_{x_j}s''} \tag{9}$$

where only the dominant source terms are retained on the right-hand side.

We note that the dilatation source terms in the transport equations for density, pressure and temperature variance represent inviscid mechanism; they are devoid of any viscous or conduction effects. These source terms are also dominated by the acoustic mode, which has isentropic thermodynamic fluctuations. The isentropic relations between p', ρ' and T' can thus be used for modeling the unclosed correlations in the respective dilatation source terms. Also note that the isentropic thermodynamic field is expected to correlate well with the dilatational velocity field, as both correspond to the acoustic waves generated at the shock wave. The fact that LIA is able to reproduce the acoustic mode, namely the pressure fluctuations, makes the linear inviscid framework appropriate for modeling the simplified transport equations given in Eqs. (6) - (8).

The dissipation term in the entropy equation shown in Eq. (9) has to be modeled differently, as the LIA theory does not provide information on the viscous and heat conduction effects. We can, however, exploit the entropy mode generated at the shock, and its isobaric nature to develop closure models for the dissipation source terms in the entropy and temperature equations. The model equations can be cast in the $k - \epsilon$ framework, in line with the modeling of the vorticity variance and the solenoidal dissipation rate in Ref. [50]. Also, the variation of the mean conductivity across shock wave has to be accounted for, akin to the effect of the mean viscosity on the turbulent dissipation rate. The new physics-based models thus developed can be applied to canonical shock-turbulence interaction cases from the current simulations as well as those of Larsson et al. [26]. The magnitude of the thermodynamic variances generated for different Mach numbers and their post-shock evolution can be compared to the extensive scDNS statistics and LIA results presented in Sect. 3.

6 Conclusion

In this work, we present shock-captured DNS data for thermodynamic fluctuations generated by canonical shock-turbulence interaction. A large parameter space in terms of Mach number is considered, and the available scDNS data is complemented with new cases computed here. The linear interaction analysis based on Kovásznay mode decomposition of the disturbances is applied under the linear inviscid framework. LIA results are compared with the scDNS data and are further used to investigate the thermodynamic field in terms of their component Kovásznay modes.

The simulations predict high values of pressure, density and temperature variances behind the shock. A new threshold method based on the instantaneous shock dilatation captures the peak thermodynamic variances by eliminating the large effect of unsteady shock motion inherent in conventional averaging at a fixed x_1 location. It gives excellent match with the near-field ($x_1 = 0^+$) LIA values. The far-field thermodynamic variances show steady increase in magnitude with increasing strength of interaction. There are interesting non-monotonic trends, for example, in the variation of the near field $\overline{\rho'^2}$ values with Mach number. The density variance generated by strong shocks ($M_u \geq 2.5$) also show a non-monotonic variation (and a local peak in magnitude) with distance from the shock wave. These are caused by the interplay between the acoustic and the entropy modes generated by the interaction.

Transport equations are written to investigate the varying post-shock evolution of the different thermodynamic variances. Shock-captured DNS data is used to compute the budget of the source terms in the flow downstream of the shock interaction for a range of Mach numbers. It is found that the budget is dominated by dilatation effect typical of the acoustics in the near field, whereas the far field variations are dominated by viscous dissipation and non-linear effects. The only exception is the entropy variance, which is independent of the acoustic decay behind the shock. The magnitude of the dissipation term is found to increase with shock strength, such that it prominently shows up for the temperature variance in the high Mach number interactions. The budget data is used to write simplified transport equations governing the thermodynamics variances. These can form the foundation for developing physics-based turbulence models for the thermodynamic fluctuations generated by the shock waves. In addition, well-validated LIA results, along with the extensive data presented in this work, can be used effectively for modeling and validation.

Acknowledgements YP thank the C-DAC NPSF PARAM YUVA-II supercomputing facility, Pune, India for providing the required computational resources. YP and KS also thank the LRZ: Leibniz Supercomputing Centre, Munich, Germany for providing computational resources as part of the 4th SFB TRR40 Summer Program 2017 held at TUM, Germany. JL is supported by the National Science Foundation (Grant CBET-1453633) and the Air Force Office of Scientific Research (Grant FA95501610385). Preliminary results of this article were presented at the *Tenth International Symposium on Turbulence and Shear Flow Phenomena (TSFP10)*, Chicago, IL, USA, 6 - 9, July 2017.

References

1. Abdikamalov, E., Zhaksylykov, A., Radice, D., Berdibek, S.: Shock-turbulence interaction in core-collapse supernovae. Mon. Not. R. Astron. Soc. **461**(4), 3864 – 3876 (2016)
2. Agui, J.H., Briassulis, G., Andreopoulos, Y.: Studies of interactions of a propagating shock wave with decaying grid turbulence: velocity and vorticity fields. J. Fluid Mech. **524**, 143–195 (2005)
3. Barre, S., Alem, D., Bonnet, J.P.: Experimental study of a normal shock / homogeneous turbulence interaction. AIAA J. **34**(5), 968 – 974 (1996)
4. Bermejo-Moreno, I., Bodart, J., Larsson, J., Barney, B.M., Nichols, J.W., Jones, S.: Solving the compressible navier-stokes equations on up to 1.97 million cores and 4.1 trillion grid points. In: Proc. Int. Conf. High Perform. Comput. Networking, Storage Anal., SC '13, pp. 62:1 – 62:10. ACM, New York, NY, USA (2013)
5. Boukharfane, R., Bouali, Z., Mura, A.: Evolution of scalar and velocity dynamics in planar shock-turbulence interaction. Shock Waves (2018)
6. Donzis, D.A.: Amplification factors in shock-turbulence interactions: effect of shock thickness. Phys. Fluids **24**(1), 011,705 (2012)
7. Donzis, D.A.: Shock structure in shock-turbulence interactions. Phys. Fluids **24**(12), 126,101 (2012)
8. Ducros, F., Laporte, F., Soulères, T., Guinot, V., Moinat, P., Caruelle, B.: High-Order Fluxes for Conservative Skew-Symmetric-like Schemes in Structured Meshes: Application to Compressible Flows. J. Comput. Phys. **161**(1), 114 – 139 (2000)
9. Fabre, D., Jacquin, L., Sesterhenn, J.: Linear interaction of a cylindrical entropy spot with a shock. Phys. Fluids **13**(8), 2403 – 2422 (2001)
10. Gerolymos, G.A., Vallet, I.: Pressure, density, temperature and entropy fluctuations in compressible turbulent plane channel flow. J. Fluid Mech. **757**, 701 – 746 (2014)
11. Griffond, J.: Linear interaction analysis applied to a mixture of two perfect gases. Phys. Fluids **17**(8), 086,101 (2005)
12. Grube, N., Taylor, E., Martin, M.P.: Direct Numerical Simulation of Shock-wave/Isotropic Turbulence Interaction. In: 39th AIAA Fluid Dyn. Conf., Fluid Dynamics and Co-located Conferences. AIAA Paper 2009-4165, San Antonio, Texas (2009)
13. Grube, N., Taylor, E., Martin, M.P.: Numerical Investigation of Shock-wave/Isotropic Turbulence Interaction. In: 49th AIAA Aerosp. Sci. Meet. Incl. New Horizons Forum Aerosp. Expo., Aerospace Sciences Meetings. AIAA Paper 2011-480, Orlando, Florida (2011)

14. Hannappel, R., Friedrich, R.: Direct Numerical Simulation of a Mach 2 shock interacting with isotropic turbulence. Appl. Sci. Res. **54**(3), 205 – 221 (1995)
15. Hesselink, L., Sturtevant, B.: Propagation of weak shocks through a random medium. J. Fluid Mech. **196**, 513 – 553 (1988)
16. Honkan, A., Watkins, C.B., Andreopoulos, J.: Experimental Study of Interactions of shock wave with free-stream turbulence. J. Fluids Eng. **116**, 763 – 769 (1994)
17. Huete, C., Wouchuk, J.G., Velikovich, A.L.: Analytical linear theory for the interaction of a planar shock wave with a two- or three-dimensional random isotropic acoustic wave field. Phys. Rev. E **85**(2), 026,312 (2012)
18. Huete Ruiz de Lira, C., Velikovich, A.L., Wouchuk, J.G.: Analytical linear theory for the interaction of a planar shock wave with a two- or three-dimensional random isotropic density field. Phys. Rev. E **83**, 056,320 (2011)
19. Jacquin, L., Blin, E., Geffroy, P.: An Experiment on Free Turbulence/Shock Wave Interaction. In: F. Durst, R. Friedrich, B.E. Launder, F.W. Schmidt, U. Schumann, J.H. Whitelaw (eds.) Turbulent Shear Flows 8: Selected Papers from the Eighth International Symposium on Turbulent Shear Flows, Munich, Germany, September 9 - 11, 1991, pp. 229 – 248. Springer Berlin Heidelberg, Berlin, Heidelberg (1993)
20. Jamme, S., Cazalbou, J., Torres, F., Chassaing, P.: Direct numerical simulation of the interaction between a shock wave and various types of isotropic turbulence. Flow, Turbul. Combust. **68**(3), 227 – 268 (2002)
21. Johnsen, E., Larsson, J., Bhagatwala, A.V., Cabot, W.H., Moin, P., Olson, B.J., Rawat, P.S., Shankar, S.K., Sjögreen, B., Yee, H.C., Zhong, X., Lele, S.K.: Assessment of high-resolution methods for numerical simulations of compressible turbulence with shock waves. J. Comput. Phys. **229**(4), 1213 – 1237 (2010)
22. Kitamura, T., Nagata, K., Sakai, Y., Sasoh, A., Ito, Y.: Changes in divergence-free grid turbulence interacting with a weak spherical shock wave. Phys. Fluids **29**(6), 065,114 (2017)
23. Kovásznay, L.S.G.: Turbulence in Supersonic Flow. J. Aeronaut. Sci. **20**(10), 657 – 674, 682 (1953). Reprinted in *AIAA J.*, **41(7)**, 219 – 237, 2003
24. Larsson, J.: Blending technique for compressible inflow turbulence: Algorithm localization and accuracy assessment. J. Comput. Phys. **228**(4), 933 – 937 (2009)
25. Larsson, J.: Effect of Shock-Capturing Errors on Turbulence Statistics. AIAA J. **48**(7), 1554 – 1557 (2010)
26. Larsson, J., Bermejo-Moreno, I., Lele, S.K.: Reynolds-and Mach-number effects in canonical shock-turbulence interaction. J. Fluid Mech. **717**, 293 – 321 (2013)
27. Larsson, J., Lele, S.K.: Direct numerical simulation of canonical shock/turbulence interaction. Phys. Fluids **21**(12), 126,101 (2009)
28. Lee, S., Lele, S.K., Moin, P.: Simulation of spatially evolving turbulence and the applicability of Taylor's hypothesis in compressible flow. Phys. Fluids A **4**(7), 1521 – 1530 (1992)
29. Lee, S., Lele, S.K., Moin, P.: Direct numerical simulation of isotropic turbulence interacting with a weak shock wave. J. Fluid Mech. **251**, 533 – 562 (1993)
30. Lee, S., Lele, S.K., Moin, P.: Interaction of isotropic turbulence with shock waves: effect of shock strength. J. Fluid Mech. **340**, 225 – 247 (1997)
31. Lee, S., Moin, P., Lele, S.K.: Interaction of isotropic turbulence with a shock wave. Tech. Rep. TF-52, Thermosciences Division, Department of Mechanical Engineering, Stanford University, Stanford, California 94305 (1992)
32. Lele, S.K.: Shock-jump relations in a turbulent flow. Phys. Fluids A **4**(12), 2900 – 2905 (1992)
33. Lele, S.K.: Compressibility Effects on Turbulence. Annu. Rev. Fluid Mech. **26**(1), 211 – 254 (1994)
34. Livescu, D., Ryu, J.: Vorticity dynamics after the shock-turbulence interaction. Shock Waves **26**(3), 241 – 251 (2016)
35. Mahesh, K., Lee, S., Lele, S.K., Moin, P.: The interaction of an isotropic field of acoustic waves with a shock wave. J. Fluid Mech. **300**, 383 – 407 (1995)
36. Mahesh, K., Lele, S.K., Moin, P.: The influence of entropy fluctuations on the interaction of turbulence with a shock wave. J. Fluid Mech. **334**, 353 – 379 (1997)
37. Mahesh, K., Moin, P., Lele, S.K.: The interaction of a shock wave with a turbulent shear flow. Tech. Rep. TF-69, Thermosciences Division, Department of Mechanical Engineering, Stanford University, Stanford, California 94305 (1996)
38. Moore, F.K.: Unsteady oblique interaction of a shock wave with a plane disturbance. Tech. Rep. NACA TR 1165, NACA (1954). Supersedes *NACA TN 2879*, 1953

39. Pirozzoli, S., Bernardini, M.: Turbulence in supersonic boundary layers at moderate Reynolds number. J. Fluid Mech. **688**, 120 – 168 (2011)
40. Pope, S.B.: Turbulent flows. Cambridge Univesity Press. Cambridge, UK (2000)
41. Quadros, R., Sinha, K.: Modelling of turbulent energy flux in canonical shock-turbulence interaction. Int. J. Heat Fluid Flow **61, Part B**, 626 – 635 (2016)
42. Quadros, R., Sinha, K., Larsson, J.: Kovasznay Mode Decomposition of Velocity-Temperature Correlation in Canonical Shock-Turbulence Interaction. Flow, Turbul. Combust. **97**(3), 787 – 810 (2016)
43. Quadros, R., Sinha, K., Larsson, J.: Turbulent energy flux generated by shock/homogeneous-turbulence interaction. J. Fluid Mech. **796**, 113 – 157 (2016)
44. Rawat, P., Zhong, X.: Direct Numerical Simulations of Turbulent Flow Interactions with Strong Shocks Using Shock-Fitting Method. In: 49th AIAA Aerosp. Sci. Meet. Incl. New Horizons Forum Aerosp. Expo., Aerospace Sciences Meetings. AIAA Paper 2011-649, Orlando, Florida (2011)
45. Ribner, H.S.: Convection of a pattern of vorticity through a shock wave. Tech. Rep. NACA TR 1164, NACA (1954). Supersedes *NACA TN 2864*, 1953
46. Ristorcelli, J.R., Blaisdell, G.A.: Consistent initial conditions for the DNS of compressible turbulence. Phys. Fluids **9**(1), 4 – 6 (1997)
47. Roy, S., Pathak, U., Sinha, K.: Variable Turbulent Prandtl Number Model for Shock / Boundary - Layer Interaction. AIAA J. **56**(1), 342 – 355 (2018)
48. Ryu, J., Livescu, D.: Turbulence structure behind the shock in canonical shock-vortical turbulence interaction. J. Fluid Mech. **756** (2014)
49. Sesterhenn, J., Dohogne, J.F., Friedrich, R.: Direct numerical simulation of the interaction of isotropic turbulence with a shock wave using shock-fitting. C. R. Méc. **333**(1), 87 – 94 (2005)
50. Sinha, K.: Evolution of enstrophy in shock/homogeneous turbulence interaction. J. Fluid Mech. **707**, 74 – 110 (2012)
51. Sinha, K., Mahesh, K., Candler, G.V.: Modeling shock unsteadiness in shock/turbulence interaction. Phys. Fluids **15**(8), 2290 – 2297 (2003)
52. Smits, A.J., Dussauge, J.P.: Turbulent Shear Layers in Supersonic Flow. Springer-Verlag. New York, USA (2005)
53. Thompson, P.A.: Compressible-Fluid Dynamics. McGraw-Hill Inc. New York, USA (1984)
54. Tian, Y., Jaberi, F.A., Li, Z., Livescu, D.: Numerical study of variable density turbulence interaction with a normal shock wave. J. Fluid Mech. **829**, 551 – 588 (2017)
55. Wang, X., Zhong, X.: Effect of compressibility on strong shock and turbulence interactions. In: 50th AIAA Aerosp. Sci. Meet. Incl. New Horizons Forum Aerosp. Expo., Aerospace Sciences Meetings. AIAA Paper 2012-3162, Nashville, Tennessee (2012)
56. Wouchuk, J.G., Huete Ruiz de Lira, C., Velikovich, A.L.: Analytical linear theory for the interaction of a planar shock wave with an isotropic turbulent vorticity field. Phys. Rev. E **79**(6), 066,315 (2009)
57. Zank, G.P., Zhou, Y., Matthaeus, W.H., Rice, W.K.M.: The interaction of turbulence with shock waves: A basic model. Phys. Fluids **14**(11), 3766 – 3774 (2002)